Earth Syst. Sci. Data, 16, 3495–3515, 2024
https://doi.org/10.5194/essd-16-3495-2024
© Author(s) 2024. This work is distributed under
the Creative Commons Attribution 4.0 License.

Open Access Earth System Science Data

Global Emissions Inventory from Open Biomass Burning (GEIOBB): utilizing Fengyun-3D global fire spot monitoring data

Yang Liu[1,2], Jie Chen[3,4], Yusheng Shi[1], Wei Zheng[3,4], Tianchan Shan[3,4], and Gang Wang[5]

[1]State Key Laboratory of Remote Sensing Science, Aerospace Information Research Institute, Chinese Academy of Sciences, Beijing 100101, China
[2]College of Resources and Environment, University of Chinese Academy of Sciences, Beijing 101408, China
[3]Innovation Center for FengYun Meteorological Satellite, National Satellite Meteorological Center (National Center for Space Weather), China Meteorological Administration, Beijing 100081, China
[4]Key Laboratory of Radiometric Calibration and Validation for Environmental Satellites, National Satellite Meteorological Center (National Center for Space Weather), China Meteorological Administration, Beijing 100081, China
[5]Guangzhou Meteorological Satellite Ground Station, National Satellite Meteorological Center (National Center for Space Weather), China Meteorological Administration, Guangzhou 510640, China

Correspondence: Yusheng Shi (shiys@aircas.ac.cn) and Tianchan Shan (shantc9165@163.com)

Received: 18 December 2023 – Discussion started: 3 January 2024
Revised: 3 June 2024 – Accepted: 16 June 2024 – Published: 2 August 2024

Abstract. Open biomass burning (OBB) significantly affects regional and global air quality, the climate, and human health. The burning of forests, shrublands, grasslands, peatlands, and croplands influences OBB. A global emissions inventory based on satellite fire detection enables an accurate estimation of OBB emissions. In this study, we developed a global high-resolution (1 km × 1 km) daily OBB emission inventory using the Chinese Fengyun-3D satellite's global fire spot monitoring data, satellite-derived biomass data, vegetation-index-derived spatiotemporally variable combustion efficiencies, and land-type-based emission factors. The average annual estimated OBB emissions for 2020–2022 were 2586.88 Tg C, 8841.45 Tg CO_2, 382.96 Tg CO, 15.83 Tg CH_4, 18.42 Tg NO_x, 4.07 Tg SO_2, 18.68 Tg particulate organic carbon (OC), 3.77 Tg particulate black carbon (BC), 5.24 Tg NH_3, 15.85 Tg NO_2, 42.46 Tg $PM_{2.5}$ and 56.03 Tg PM_{10}. Specifically, taking carbon emissions as an example, the average annual estimated OBBs for 2020–2022 were 72.71 (Boreal North America, BONA), 165.73 (Temperate North America, TENA), 34.11 (Central America, CEAM), 42.93 (Northern Hemisphere South America, NHSA), 520.55 (Southern Hemisphere South America, SHSA), 13.02 (Europe, EURO), 8.37 (Middle East, MIDE), 394.25 (Northern Hemisphere Africa, NHAF), 847.03 (Southern Hemisphere Africa, SHAF), 167.35 (Boreal Asia, BOAS), 27.93 (Central Asia, CEAS), 197.29 (Southeast Asia, SEAS), 13.20 (Equatorial Asia; EQAS), and 82.38 (Australia and New Zealand; AUST) Tg C yr^{-1}. Overall, savanna grassland burning contributed the largest proportion of the annual total carbon emissions (1209.12 Tg C yr^{-1}; 46.74 %), followed by woody savanna/shrubs (33.04 %) and tropical forests (12.11 %). SHAF was found to produce the most carbon emissions globally (847.04 Tg C yr^{-1}), followed by SHSA (525.56 Tg C yr^{-1}), NHAF (394.26 Tg C yr^{-1}), and SEAS (197.30 Tg C yr^{-1}). More specifically, savanna grassland burning was predominant in SHAF (55.00 %, 465.86 Tg C yr^{-1}), SHSA (43.39 %, 225.86 Tg C yr^{-1}), and NHAF (76.14 %, 300.21 Tg C yr^{-1}), while woody savanna/shrub fires were dominant in SEAS (51.48 %, 101.57 Tg C yr^{-1}). Furthermore, carbon emissions exhibited significant seasonal variability, peaking in September 2020 and August of 2021 and 2022, with an average of 441.32 Tg C $month^{-1}$, which is substantially higher than the monthly average of 215.57 Tg C $month^{-1}$. Our comprehensive high-resolution inventory of OBB emissions provides valuable insights for enhancing the accuracy of air quality modeling, atmospheric transport, and

biogeochemical cycle studies. The GEIOBB dataset can be downloaded at http://figshare.com (last access: 30 July 2024) with the following DOI: https://doi.org/10.6084/m9.figshare.24793623.v2 (Liu et al., 2023).

1 Introduction

Open biomass burning (OBB) releases significant amounts of trace gases (CO, NO_x, NMVOC, SO_2, and NH_3), particulate matter ($PM_{2.5}$, PM_{10}), and greenhouse gases (CH_4 and CO_2), which are major atmospheric pollutants (Mehmood et al., 2022) and have profound impacts on the global carbon cycle, climate, and air quality, thus exerting a significant influence on the global environment and human health (Wu et al., 2022). The burning of forests, shrublands, grasslands, crop residues, and peatland constitutes the major types of fires worldwide (van der Werf et al., 2017). These open-burning activities severely affect air quality and ecosystems (Chen et al., 2017), with high degrees of sporadicity and spatiotemporal clustering (Liu et al., 2014; Murdiyarso and Lebel, 2007; Senande-Rivera et al., 2022). In addition, some regions worldwide are experiencing a notable increase in fire incidents (Kolden et al., 2024; Richardson et al., 2022), such as the Amazon rainforest (Pivello, 2011), Australian bush (Jegasothy et al., 2023), and the United States (You and Xu, 2023), where large-scale fire incidents occur periodically and frequently (Kolden et al., 2024). Therefore, accurately estimating these emissions is crucial for devising effective environmental policies and safeguarding human health and quality of life, thereby providing significant support for a sustainable future.

Previous studies have investigated numerous methods for estimating biomass-burning emissions (Ito and Penner, 2004; Wiedinmyer et al., 2006). The burned-area-based fire emission estimation method, which is based on the burned area, available biomass fuels burned in the fields, fuel-related combustion efficiency, and emission factors, has demonstrated good accuracy in quantifying larger fire events. This method has been widely used in databases such as the Global Fire Emissions Database (GFED) (van der Werf et al., 2017) and the Fire INventory from NCAR (FINN) (Wiedinmyer et al., 2023). However, this method relies heavily on the fire-detection precision, particularly for small fires. A method based on fire radiative power (FRP) can enhance the detection and quantification of small-fire events by measuring the energy released during combustion (Filizzola et al., 2023). However, these approaches can overestimate emissions from localized fire events, which are intense small-scale fires that may not reflect wider fire activity (Nguyen et al., 2023). For example, Fire Energetics and Emissions Research (FEER), based on FRP, reported that the global total particulate matter emissions were approximately 55 % higher than those estimated by the GFED (Ichoku and Ellison, 2014). Similarly, the Global Fire Assimilation System (GFAS) used estimated global and regional combustion FRP values, exceeding those of the GFED by approximately 126 $Tg\,C\,yr^{-1}$ during 2003–2008 (Kaiser et al., 2012). However, all these methods rely on MODIS active fire products.

Similar to the MERSI-2 instrument, the Fengyun-3D (FY-3D) satellite has spatial resolutions of 250 m (0.47–0.86 µm and 10.80–12.02 µm) and 1000 m (1.38–8.55 µm) at the nadir (Yin et al., 2020), which is more advantageous in detecting and monitoring various active fire events compared with MODIS (Zheng et al., 2023). Furthermore, the global fire monitoring (GFR) product of FY-3D employs optimized automatic identification algorithms for fire spots (Shan and Zheng, 2022), leading to improved fire point detection accuracy. Thus, it has an overall accuracy rate of 79.43 % and exclusion omission error accuracy of 88.50 %, surpassing the capabilities of MODIS satellite products (Chen et al., 2022; Xian et al., 2021) based on field-collected references from China throughout 2020. Cross-verification between MODIS and FY-3D showed the highest consistency (over 80 %) in Africa and Asia, whereas the consistency in America, Europe, and Oceania exceeded 70 % (Chen et al., 2022). The number of fire spots in July, August, and September was higher, with a mean consistency of over 85 % between MODIS and FY-3D fire products (Chen et al., 2022). Although the Landsat Fire and Thermal Anomaly (LFTA) product has a finer spatial resolution, its lower temporal resolution limits its global coverage to only 16 d; thus, large numbers of fires with short durations are missed. The shorter revisit time of FY-3D allows for monitoring more fires lasting for 1 d, which are expected to yield reliable estimates of OBB emissions.

Fuel loading (F) represents the ground biomass of the fire-affected pixels. Many studies have adopted a static approach to F (Chang and Song, 2010; Puliafito et al., 2020; Shi et al., 2020; Zhou et al., 2017), assigning constant values based on regional land-cover types. This methodology overlooks the inherent spatial and temporal variability in F within each land type, which changes continuously and dynamically (Wiedinmyer et al., 2011). The combustion factor (CF), which denotes the ratio of consumed fuel to total available fuels, is typically a linear variable within a specific range when considering the fuel status and humidity conditions (van der Werf et al., 2006; Wiedinmyer et al., 2011). However, this approach to calculating CF leads to increased uncertainty in biomass estimation and poor quantification of the extent of combustion during fire events, thereby affecting OBB emissions assessment (Shi et al., 2020). To address these issues, this study employed observational and satellite-based aboveground biomass (AGB) and CF based on time

series vegetation index data derived from satellite products. The CF considers moisture-related factors, enabling the calculation of the spatiotemporal variance in combustion efficiency across diverse land types.

This study aimed to develop a high-resolution daily OBB emissions inventory – including carbon (C), carbon dioxide (CO_2), carbon monoxide (CO), methane (CH_4), nitrogen oxides (NO_x), sulfur dioxide (SO_2), particulate organic carbon (OC), particulate black carbon (BC), ammonia (NH_3), nitrogen dioxide (NO_2), $PM_{2.5}$, and PM_{10} – and analyze the various types of fire events along with their emission patterns across 14 distinct regions. To estimate the OBB emissions from forests, savannas/shrublands, grasslands, and peatlands, we utilized the updated FY-3D GFR product based on the continuous spatiotemporal dynamics of AGB, spatially and temporally variable combustion efficiencies, and emission factors specific to different land types. Our comprehensive high-resolution inventory of OBB emissions represents a valuable asset for applications in air quality modeling, atmospheric transport simulations, and biogeochemical cycling studies. This provides a robust framework for in-depth understanding and analysis of the environmental implications of OBB on a global scale.

2 Materials and methods

The Global Emissions Inventory from Open Biomass Burning (GEIOBB) (1 km daily) was estimated using the burned area method based on the framework described by Wiedinmyer et al. (2006) and Shi et al. (2015). GEIOBB includes OBB emissions based on burned areas retrieved from active fire data from the FY-3D satellite, available biomass from satellite and ground measurements, CF scaled by tree cover (TC) and the normalized difference vegetation index (NDVI), and land-cover-based (LC-based) emission factors. GEIOBB is obtained by calculating the product of the above terms:

$$E_i(x) = B(x,t) \times F(x) \times \mathrm{CF}(x) \times \mathrm{EF}(i), \quad (1)$$

where E_i (g) represents emissions of pollutant type i at location x, which is equal to the product of burning area, B (m^2), at time t and location x; biomass F ($kg\,m^{-2}$) at location x; CF (expressed as a fraction); and the emission factor, EF ($g\,kg^{-1}$), for pollutant type i.

2.1 FY-3D global fire-spot-monitoring-data-based burned area (B)

The Fengyun-3 series of satellites is a second-generation Chinese polar-orbiting meteorological satellite system. The FY-3D satellite was the fourth in the FY-3 series. It was launched on 15 November 2017 at an altitude of 836 km and the data became accessible in May 2020 (Li et al., 2017). FY-3D completes 14 orbital observations of the Earth's surface on a global scale twice daily. The MERSI-2 instrument onboard FY-3D was a significant improvement compared with the MERSI-1 instrument onboard FY-3C, with high onboard accuracy and lunar calibration capabilities. Compared with MODIS, FY-3D fire products have been optimized in terms of auxiliary parameters, fire identification, and re-identification. First, FY-3D introduces an adaptive threshold using automatic identification algorithms for fire spot detection, which calculates the background temperature as the mean temperature of all the background pixels within each 3×3 window. If fewer than 20 % of the pixels are identified as cloudless, the window size is expanded to 5×5, continuing up to 51×51 in order to accommodate more data (Chen et al., 2022). This approach eliminates the limitations in the MODIS and Visible Infrared Imaging Radiometer Suite (VIIRS) algorithms, which set T4 (4 µm brightness temperatures) to a value greater than fixed 360 K (320 K at night) and the variable moving window size to a maximum of 21×21 (Giglio et al., 2016). Second, FY-3D uses a re-identification index that reflects varying geographical latitudes and underlying surface types together with the effects of clouds, water, and bare land (Zheng et al., 2020). Based on the initially identified fire spots, FY-3D employed the re-identification index to further remove false fire spots at cloud edges, waterbody edges, and other high-reflection underlying surfaces (Chen et al., 2022). The integration of multiple influencing factors increases the fire detection accuracy. For example, the influences of factory thermal anomalies and high reflectance of photovoltaic power plants are removed. Finally, FY-3D employs a far-infrared band with a high resolution of 250 m, which has a higher resolution than MODIS (1 km) (Zheng et al., 2023). The far-infrared band has a higher sensitivity to large fires or high-brightness fire events and can distinguish between background brightness temperatures (Zheng and Chen, 2020). These characteristics are essential for the accurate identification of fire spots, thereby enhancing the fire detection precision of satellites (Chen et al., 2022). Overall, the FY-3D GFR product has an accuracy of 94.01 % globally, as calculated using fire detection after eliminating errors based on visual checks conducted using SMART (Satellite Monitoring Analyzing and Remote sensing Tools, visual check) in 2019. It achieves accuracies of 94.61 %, 94.12 %, 90.63 %, 91.76 %, and 92.69 % for southern central Africa, eastern central South America, Siberia, Australia, and the Indochinese Peninsula, respectively (Chen et al., 2022). Specifically, owing to the removal of the underlying surface interference in China, FY-3D achieves 79.43 % and 88.50 % accuracy (with fire omitted) and accuracy without omission (misidentified fire) (Chen et al., 2022). These accuracies were determined by comparing the results of a large-scale field experiment conducted jointly by the State Grid Corporation of China and China Meteorological Administration with the GFR product, including both omitted and misidentified fire (Chen et al., 2022). This comprehensive assessment took place throughout 2020 across five provinces in China – Guangdong, Guangxi, Yunnan, Guizhou, and Hainan – uti-

lizing a combination of real-time satellite data and ground truth validation to evaluate the suitability of these fire detection products. These accuracies are significantly higher than those achieved by MODIS, which are 74.23 % and 79.69 %, respectively (Chen et al., 2022).

The location, timing, and burned area of the fire events used in GEIOBB were determined globally using the FY-3D GFR product (Chen et al., 2022). Processed fire event detection data are from the Fengyun Satellite Remote Sensing Data Service Network of National Satellite Meteorological Centre (http://satellite.nsmc.org.cn/PortalSite/Default.aspx, last access: 30 July 2024), which estimated the actual area of fire spots based on radiation in different infrared channels. When the mid-infrared channel was not saturated, it was used to estimate the sub-pixel fire spot area and temperature. Otherwise, a far-infrared channel was employed for the estimation (Zheng and Chen, 2020). These data offer daily fire detection at a 1 km resolution, including the location, time, burned area, and confidence level (Liu and Shi, 2023). Furthermore, multiple counts of the same fire may have been recorded on a single day, leading to data duplication. To address this issue, we performed a global identification and removed multiple daily detections of the same fire pixels and data with confidence levels below 20 %. Specifically, we removed single daily fire detections within a 1 km radius of another fire detection. Thus, only one fire per 1 km^2 of a hotspot could be counted per day and was reset on the next day (Wiedinmyer et al., 2023).

2.2 Fuel loading (F)

Previous studies based on burned areas have distinguished F by categorizing it according to regions of different fire types (Wiedinmyer et al., 2011). The data generated by this method have some discontinuities, which may lead to large deviations at the boundaries of different areas; this is unreasonable and does not reflect the spatial distribution pattern of F. Ground observation data are more accurate and reliable, but are limited by the sparse distribution of observation stations, preventing comprehensive global coverage. In contrast, satellite data cover the entire globe and provide worldwide surface parameters, thereby enabling biomass estimation. However, their accuracy and usability are limited by factors such as their temporal and spatial resolutions and cloud cover. Therefore, combining ground observations with satellite data is an effective solution. This fusion method combines the high accuracy of ground observation data with the wide coverage of satellite data to generate global biomass products. Using this method, it is possible to overcome the limitations of using a single data source, thereby enhancing the accuracy of biomass estimations.

This study used multi-source data, including NDVI, TC, and AGB, to assess the terrestrial biomass. NDVI data were obtained using the MODIS combined 16 d NDVI fusion product, which is available on the Google Earth Engine platform. AGB shows a strong linear correlation with TC and NDVI (Yao et al., 2017). The TC data were derived from the MOD44B product (DiMiceli et al., 2022), which is generated based on MODIS on board the Terra satellite (https://lpdaac.usgs.gov/products/mod44bv061/, last access: 30 July 2024), which provides a continuous global vegetation field at 250 m resolution for each year from 2000 to the present. AGB data were obtained from the Global Aboveground and Belowground Biomass Carbon Density Maps for the Year 2010 product (https://daac.ornl.gov/cgi-bin/dsviewer.pl?ds_id=1763, last access: 30 July 2024), which is provided by Spawn and Gibbs (2020). This dataset uses thousands of satellite data points and ground measurements to produce a biomass map with a 1 km resolution (Spawn and Gibbs, 2020). A combination of 2118 other ground measurements and lidar data was used to validate observations and showed that the fused map had a root-mean-square error (RMSE) that was 15 %–21 % lower than those reported by Saatchi et al. (2011) and Baccini et al. (2012). We used the AGB for 2010, annual TC, and NDVI data and linearly stretched the fuel loading to other years.

$$F(x,t) = \left(\frac{\mathrm{NDVI_{now}} + \mathrm{TC_{now}}}{\mathrm{NDVI_{2010}} + \mathrm{TC_{2010}}}\right) \times \mathrm{AGB}, \quad (2)$$

where $\mathrm{NDVI_{now}}$ is the mean value of the month before a single fire event, $\mathrm{NDVI_{2010}}$ is the mean value of NDVI in 2010, $\mathrm{TC_{now}}$ is the tree cover in the year of the fire incident, $\mathrm{TC_{2010}}$ is the tree cover in 2010, and AGB is the aboveground biomass in 2010.

2.3 Combustion factor (CF)

The CF is mainly defined as the percentage of fuel consumed during individual fire events, which primarily depends on the type of fuel and humidity. Typically, the CF is set as a linear variable within a specific range, which may lead to biases in emission estimations and generate significant uncertainties. Although some studies used TC to quantify CF and explain its spatial and temporal variations (Bray et al., 2018; Qiu et al., 2016; Wiedinmyer et al., 2006; Wu et al., 2018), previous research has mainly focused on areas with herbaceous vegetation cover, where the TC ranges from 40 % to 60 %. They assumed that the CF remained consistent across other land types, such as farmlands, forests, and grasslands. The fire type at the location of the fire event has a major influence on OBB. We used data categorized by the International Geosphere–Biosphere Programme (IGBP) from the MODIS land-cover type (LCT) information (Friedl and Sulla-Menashe, 2022) (MCD12Q1; https://lpdaac.usgs.gov/products/mcd12q1v061/, last access: 30 July 2024). We reclassified the original 17 classifications into seven categories to better differentiate fire types; grasslands and savannas (V1), woody savannas or shrubs (V2), tropical forests (V3), temperate forests (V4), boreal forests (V5), temperate evergreen forests (V6), and crops (V7); this

was to allow for better matching in the calculation and subsequent analysis processes. In GEIOBB, the CF of all fires in each grid cell was allocated as a function of TC, fire type, and NDVI (Ito and Penner, 2004). We segmented the reclassification results into four categories to calculate the CF. Specifically, we amalgamated the reclassification outcomes of V3, V4, V5, and V6 into forest types, designated V1 as grassland, classified V2 as woodland, and categorized V7 as cropland (the specific classification method is detailed in Table S1 in the Supplement).

For woodland fires, CF is highly correlated with TC (Ito and Penner, 2004):

$$\mathrm{CF}_{\mathrm{woodland}} = \exp(-0.013 \times \mathrm{TC}). \quad (3)$$

For grassland fires, a change in the NDVI is usually associated with the occurrence of fires, especially in dry seasons or in areas prone to wildfires. Generally, a decrease in NDVI may indicate deteriorating vegetation health, which increases the risk of fires because dry or withered vegetation is more prone to burning. We introduced the vegetation condition index (VCI) to determine the fuel moisture conditions, which were used to measure the vegetation drought conditions by calculating contemporaneous changes in NDVI as a metric for assessing the contemporaneous conditions of vegetation. We supplemented our research based on Ito and Penner (2004) by replacing the percentage of green grass from the total grass with the VCI, which was computed using the NDVI with a time interval of 16 d at a spatial resolution of 1 km for the period of 2020–2022. In addition, we introduced a compensatory term to mitigate the impact of tree cover on grassland fires:

$$\mathrm{VCI} = \frac{\mathrm{NDVI}_{\mathrm{now}} - \mathrm{NDVI}_{\mathrm{min}}}{\mathrm{NDVI}_{\mathrm{max}} - \mathrm{NDVI}_{\mathrm{min}}}, \quad (4)$$

$$\mathrm{CF}_{\mathrm{grassland}} = (0.9 - \mathrm{TC}) \times (-2.13 \times \mathrm{VCI} + 1.38) + \mathrm{TC}, \quad (5)$$

where $\mathrm{NDVI}_{\mathrm{now}}$ is the mean value of the month before a single fire event, $\mathrm{NDVI}_{\mathrm{max}}$ is the maximum value of NDVI for the same period in the previous 3 years of the fire event, and $\mathrm{NDVI}_{\mathrm{min}}$ is the minimum value of NDVI for the same period in the previous 3 years of the fire event.

For forest fires, we used moisture category factors (MCFs) to measure forest moisture and conducted an analysis based on the partitioning of MCF values (0.33 as being very dry, 0.5 as dry, 1 as moderate, 2 as moist, 3 as wet, and 5 as very wet) provided by Anderson et al. (2004). We used the VCI as a criterion for assessing wetness and dryness and discovered that it approximately conformed to the power function distribution characteristics of VCI. Subsequently, a power function fitting was performed ($R^2 = 0.94$) through which we determined the CF:

$$\mathrm{MCF} = 0.1759 \times e^{3.5181 \times \mathrm{VCI}}, \quad (6)$$

$$\mathrm{CF}_{\mathrm{forest}} = (1 - e^{-1})^{\mathrm{MCF}}. \quad (7)$$

Most fires in croplands are artificially active, resulting in full combustion processes that are not designed for woody fuels. Therefore, we set the CF for crops to 0.98, which is the upper limit proposed by Wiedinmyer et al. (2006).

2.4 Emission factor (EF)

EFs are used to convert dry matter burned into trace gas and aerosol emissions, and this conversion denotes the number of pollutants released per unit of fuel burned. The measurements of EFs in different regions for grasslands and savannas, woody savannas or shrubs, tropical forests, temperate forests, temperate evergreen forests, and crops were reviewed and tabulated by Akagi et al. (2011), whereas those for boreal forest fires were obtained from the averages reported by Akagi et al. (2011) and Urbanski (2014). The EFs for maize, sugar, and rice crop fires were taken from the averages reported by Akagi et al. (2011), Fang et al. (2017), Liu et al. (2016), Santiago-De La Rosa et al. (2018), and Stockwell et al. (2015). The BC EFs of BC for crop fires were sourced from Kanabkaew and Kim Oanh (2011) and those for wheat fires were obtained from Cao et al. (2008). In addition, the emission factors of NO_2, $PM_{2.5}$, and PM_{10} for the crop fire were derived from Li et al. (2007) and the EF from the crop was the average of maize, sugar, rice, and wheat. The EF values are presented in Table 1.

3 Results and discussions

3.1 Spatial map of OBB emission estimates

We estimated global OBB emissions using GEIOBB, and the average annual values for 2020–2022 were 2586.88 Tg C, 3.77 Tg BC, 15.83 Tg CH_4, 382.96 Tg CO, 8841.45 Tg CO_2, 5.24 Tg NH_3, 15.85 Tg NO_2, 18.42 Tg NO_x, 18.68 Tg OC, 56.03 Tg PM_{10}, 42.46 Tg $PM_{2.5}$, and 4.07 Tg SO_2 (Table 2). Taking carbon as an example, the annual carbon emissions from the OBB were estimated for the period 2020–2022 (Fig. 1) and the total OBB emissions reached 7760.63 Tg C. The average annual carbon emissions during this period were 2586.88 Tg. Overall, clear spatial variations in the OBB carbon emissions were observed across Africa and certain regions of the Americas and Asia. In Central and South America, elevated emissions were observed in central and northeastern Brazil, northern Bolivia, northern Paraguay, eastern Mexico, and Honduras. In Africa, substantial OBB emissions originate from central Africa (excluding the Democratic Republic of the Congo), the northern regions of west Africa, and the southern regions of east Africa, where most 1 km × 1 km grid cells exhibit annual average carbon emissions exceeding 50 g C m^{-2}. Elevated carbon emissions were observed

Table 1. Emission factor (in $g\,kg^{-1}$) of different species.

Species	Grasslands and savannas	Woody savannas or shrubs	Tropical forests	Temperate forests	Boreal forests	Temperate evergreen forests	Crop			
							Maize	Sugar	Rice	Wheat
C	488.31	489.41	491.77	468.31	478.88	493.18	687.09	323.35	368.04	429.17
CO_2	1686[a]	1681[a]	1643[a]	1510[a]	1565[b]	1623[a]	2327[c]	1130[c]	1177[c]	1470[e]
CO	63.00[a]	67.00[a]	93.00[a]	122.00[a]	111.00[b]	112.00[a]	114.70[c]	34.70[c]	93.00[c]	60.00[e]
CH_4	2.00[a]	3.00[a]	5.10[a]	5.61[a]	6.00[b]	3.40[a]	4.40[c]	0.40[c]	9.59[c]	3.40[e]
NO_x	3.90[a]	3.65[a]	2.60[a]	1.04[a]	0.95[b]	1.96[a]	4.30[c]	2.60[c]	2.28[c]	3.30[e]
SO_2	0.90[a]	0.68[a]	0.40[a]	1.10[a]	1.00[b]	1.10[a]	0.44[c]	0.22[c]	0.18[c]	0.85[e]
OC	2.60[a]	3.70[a]	4.70[a]	7.60[a]	7.80[b]	7.60[a]	2.25[c]	3.30[c]	2.99[c]	3.90[d]
BC	0.37[a]	1.31[a]	0.52[a]	0.56[a]	0.20[b]	0.56[a]	0.78[d]	0.82[d]	0.52[d]	0.52[d]
NH_3	0.56[a]	1.20[a]	1.30[a]	2.47[a]	1.80[b]	1.17[a]	0.68[c]	1.00[c]	4.10[c]	0.37[e]
NO_2	3.22[a]	2.58[a]	3.60[a]	2.34[a]	0.63[b]	2.34[a]	2.99[f]			
$PM_{2.5}$	7.17[a]	7.10[a]	9.90[a]	15.00[a]	18.40[b]	17.90[a]	6.43[f]			
PM_{10}	7.20[a]	11.4[a]	18.50[a]	16.97[a]	18.40[b]	18.40[a]	7.02[f]			

All values of C were calculated using CO_2, CO, and CH_4 values. [a] Denotes the average value from Akagi et al. (2011). [b] Denotes the average from Akagi et al. (2011) and Urbanski (2014). [c] Denotes the average from Akagi et al. (2011), Fang et al. (2017), Liu et al. (2016), Santiago-De La Rosa et al. (2018), and Stockwell et al. (2015). [d] From Kanabkaew and Kim Oanh (2011). [e] From Cao et al. (2008). [f] From Li et al. (2007).

in Southeast Asia (Indochinese Peninsula), with significant emissions detected in western and eastern Myanmar, northern Laos, eastern Cambodia, southern Nepal, and parts of northern India. Notable carbon emissions were also observed in Equatorial Asia, south Sumatra, south Kalimantan, and southern Papua New Guinea.

We divided the world into 14 regions for analysis and discussion; the geographical regions were the same as those used by van der Werf et al. (2017) (Fig. 2a). As delineated by the reclassification in Fig. 2b, savanna grasslands emerged as the predominant LCT worldwide, encompassing 53.30 % of the total area. This type primarily occurs in South America, Africa, and Asia. Following closely is the woody savanna, accounting for 19.74 % of the global coverage. They are predominantly situated in Boreal Asia, Australia, selected areas of southern Africa, and parts of North America. The third most prevalent type was tropical forest, comprising 9.03 % of the total area, which is mainly distributed in South America, particularly within the Amazon rainforest, regions adjacent to the African Equator, and Southeast Asia. Other LCTs, such as temperate forest, boreal forest, temperate evergreen forest, and crops, are less extensively spread and exhibit a more dispersed distribution.

This study then quantified the estimated global average annual OBB carbon emissions from different regions and fire types during 2020–2022 (Table 3). Southern Hemisphere Africa (SHAF) was found to be the primary source of global OBB carbon emissions (847.04 Tg; 32.74 %); this trend also held true for other pollutants. Southern Hemisphere South America (SHSA) and Northern Hemisphere Africa (NHAF) ranked second and third, accounting for 20.12 % (520.55 Tg) and 15.24 % (394.26 Tg), respectively. The contributions of each fire type to the global OBB carbon emissions were then quantified. Savanna grasslands were the largest contributor (1209.12 Tg; 46.74 %), followed by woody savanna/shrubs (854.71 Tg; 33.04 %), tropical forest (313.32 Tg; 12.11 %), temperate forest (92.65 Tg; 3.58 %), crop (58.06 Tg; 2.24 %), temperate evergreen forest (41.65 Tg; 1.61 %), and boreal forest (17.37 Tg; 0.67 %). According to GFED4.1s, the annual average carbon emissions from wildfires in SHAF, SHSA, and NHAF during 2020–2022 were 1271.63 $Tg\,yr^{-1}$, accounting for approximately 64.55 % of the global total OBB carbon emissions. Their research findings are similar to the results of this study, which recorded 1761.84 Tg, equivalent to 68.10 % of the total.

Specifically, the contributions of the seven fire types to OBB carbon emissions varied dramatically across continents (van der Werf et al., 2010). In SHAF, the primary sources of OBB were savanna grasslands and woody savanna or shrubs, contributing 465.85 (54.99 %) and 324.08 $Tg\,yr^{-1}$ (38.26 %), respectively, which is consistent with Nguyen et al. (2023). Unlike in SHAF, OBB in SHSA primarily originated from savanna grasslands and tropical forests (Shi et al., 2015), contributing 225.86 (43.38 %) and 177.17 $Tg\,yr^{-1}$ (34.03 %) to the region's carbon emissions, respectively. This variation could be associated with the ecological and climatic conditions unique to each region (Sahu and Sheel, 2014; Santana et al., 2016). South America hosts the world's largest rainforests and is known for its rich biodiversity and biomass (Fagua and Ramsey, 2019). However, they are severely threatened by human-induced deforestation and forest fires (Chen et al., 2013). Studies indicate that forest fires

Table 2. Global OBB annual emissions and region-specific average annual emissions during 2020–2022 (in Tg species yr^{-1}).

	C	BC	CH_4	CO	CO_2	NH_3	NO_2	NO_x	OC	PM_{10}	$PM_{2.5}$	SO_2
2020	2861.05	4.09	17.39	423.12	9777.79	5.76	17.58	20.37	20.64	61.59	47.18	4.54
2021	2991.16	4.52	18.22	439.67	10 226.55	6.11	18.17	21.36	21.64	64.76	48.89	4.70
2022	1908.42	2.69	11.87	283.09	6520.04	3.87	11.82	13.53	13.74	41.76	31.31	2.97
Average	2586.88	3.77	15.83	381.96	8841.46	5.24	15.85	18.42	18.68	56.03	42.46	4.07
BONA	72.71	0.16	0.49	10.92	248.08	0.18	0.36	0.49	0.63	1.80	1.29	0.11
TENA	165.73	0.30	1.02	26.14	563.78	0.38	0.92	1.11	1.45	3.98	3.18	0.28
CEAM	34.11	0.06	0.23	5.21	116.26	0.08	0.20	0.23	0.27	0.81	0.56	0.05
NHSA	42.93	0.06	0.28	6.42	146.58	0.08	0.28	0.30	0.31	1.01	0.70	0.06
SHSA	520.55	0.61	3.74	83.09	1767.83	1.12	3.42	3.45	4.01	13.00	9.08	0.74
EURO	13.02	0.02	0.09	2.02	44.33	0.03	0.08	0.09	0.09	0.26	0.22	0.02
MIDE	8.37	0.01	0.06	1.28	28.54	0.02	0.05	0.06	0.05	0.15	0.13	0.01
NHAF	394.25	0.41	2.05	54.58	1354.19	0.62	2.56	2.99	2.39	7.01	6.01	0.66
SHAF	847.03	1.28	4.52	116.23	2910.72	1.52	5.17	6.40	5.55	16.48	12.82	1.38
BOAS	167.35	0.31	0.98	23.57	573.90	0.35	0.93	1.22	1.22	3.53	2.68	0.27
CEAS	27.93	0.04	0.21	4.55	94.68	0.08	0.17	0.19	0.20	0.56	0.47	0.04
SEAS	197.29	0.37	1.54	32.49	668.10	0.55	1.16	1.26	1.71	5.24	3.50	0.28
EQAS	13.20	0.03	0.10	2.04	44.94	0.03	0.08	0.09	0.11	0.36	0.22	0.02
AUST	82.38	0.11	0.52	13.41	279.54	0.19	0.48	0.54	0.70	1.83	1.59	0.15

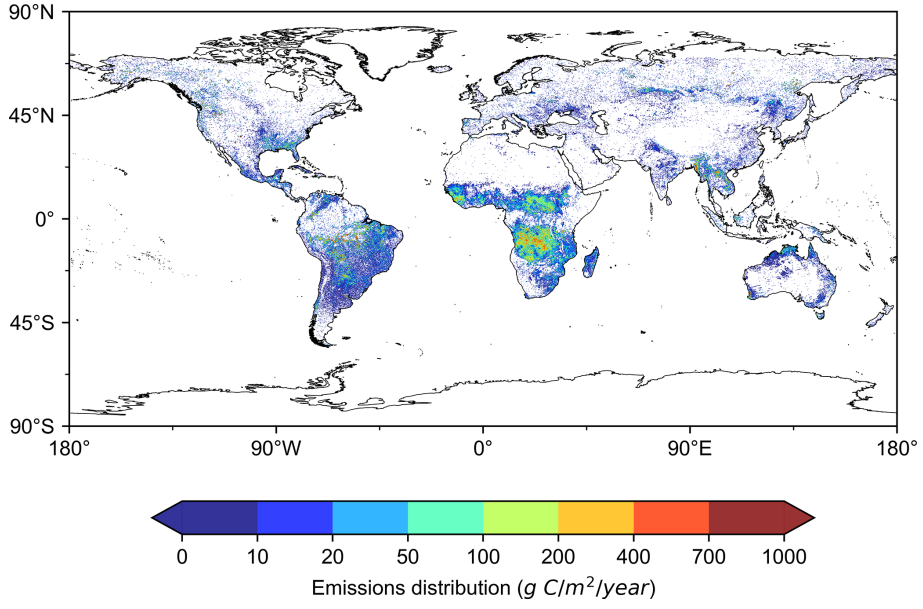

Figure 1. Spatial distribution of annual average OBB carbon emissions (1 km × 1 km) during 2020–2022.

and human activities, such as deforestation and land-use changes, are the main drivers of increased carbon emissions from OBB in this region (Cochrane and Laurance, 2002; Nepstad et al., 1999). In NHAF, the predominant source of OBB were savanna grasslands (Roberts et al., 2009), contributing 76.14 % to the region's total biomass-burning carbon emissions, averaging 300.21 Tg yr^{-1}. This may be related to the arid climate and low forest cover in the region (De Sales et al., 2016; Ichoku et al., 2016). Previous research has shown that climate change and human activities, such as grazing and agricultural expansion, are major factors in this region (Flannigan et al., 2009; Scholes and Andreae, 2000).

Fire events in savanna grasslands remain a major source of most pollutants generated by global OBB, whereas crops contribute relatively less (Fig. 3). However, with respect to BC and NH_3, fire events in woody savanna/shrubs have become the primary contributors (59.40 % for BC; 39.33 % for NH_3). Furthermore, when considering the different re-

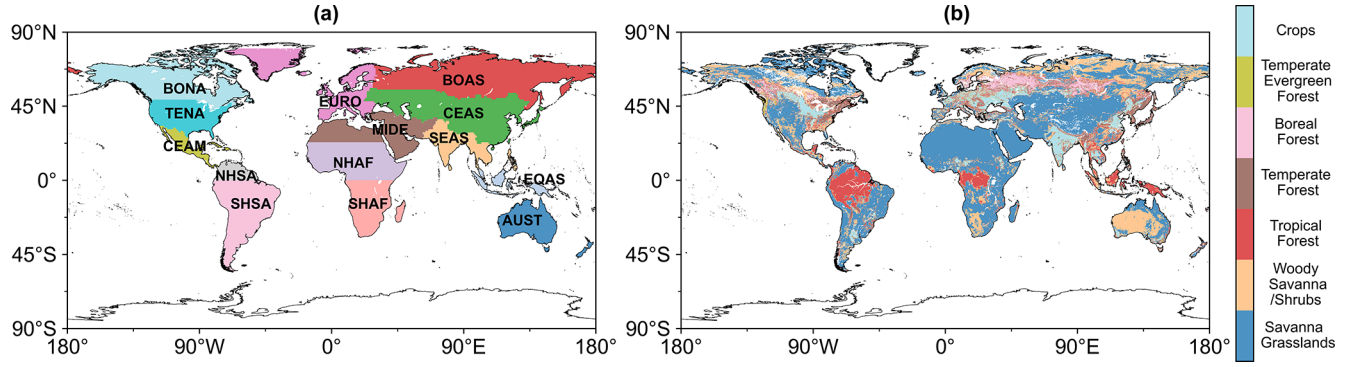

Figure 2. **(a)** Global geographic regions and its abbreviations. BONA: Boreal North America; TENA: Temperate North America; CEAM: Central America; NHSA: Northern Hemisphere South America; SHSA: Southern Hemisphere South America; EURO: Europe; MIDE: Middle East; NHAF: Northern Hemisphere Africa; SHAF: Southern Hemisphere Africa; BOAS: Boreal Asia; CEAS: Central Asia; SEAS: Southeast Asia; EQAS: Equatorial Asia; and AUST: Australia and New Zealand. **(b)** Global land-cover type reclassification.

Table 3. Annual carbon emissions from global OBB in different regions during 2020–2022 (in $\mathrm{Tg\,yr^{-1}}$).

Region	Savanna grasslands	Woody savanna/shrubs	Tropical forest	Temperate forest	Boreal forest	Temperate evergreen forest	Crop	Total
BONA	4.43	57.55	0.00	0.36	7.58	2.15	0.63	72.70
TENA	41.20	83.89	0.00	5.71	0.00	30.85	4.07	165.72
CEAM	8.62	17.47	4.57	2.33	0.00	0.02	1.11	34.12
NHSA	19.12	11.08	12.23	0.28	0.00	0.00	0.22	42.93
SHSA	225.86	76.69	177.17	27.49	0.00	0.37	12.98	520.56
EURO	5.21	4.60	0.00	0.71	0.19	0.40	1.92	13.03
MIDE	4.95	1.17	0.00	0.15	0.00	0.33	1.78	8.38
NHAF	300.21	47.03	30.31	3.93	0.00	0.00	12.78	394.26
SHAF	465.86	324.09	41.17	12.70	0.00	0.00	3.22	847.04
BOAS	59.51	95.97	0.00	1.29	9.01	0.07	1.50	167.35
CEAS	10.31	7.71	0.68	1.86	0.59	0.33	6.45	27.93
SEAS	21.46	101.57	42.39	22.26	0.00	0.26	9.36	197.30
EQAS	1.43	7.23	4.45	0.02	0.00	0.00	0.08	13.21
AUST	40.95	18.66	0.35	13.57	0.00	6.86	1.97	82.36

gions, the primary sources of pollutants from OBB vary. For instance, fire events in woody savanna/shrubs were the primary sources in the BONA, SEAS, and EQAS regions, whereas crop-related fire events mainly occurred in the EURO, MIDE, CEAS, and SEAS regions.

3.2 Temporal variations in OBB carbon emissions

The monthly carbon emissions at both global and regional levels are illustrated in Fig. 4. Overall, global OBB carbon emissions experienced notable shifts, with considerable monthly variations from 2020 to 2022, and peak emissions were observed in August 2021 (729.37 Tg). Global OBB carbon emissions were 2861.05 Tg in 2020, rising slightly to 2991.15 Tg in 2021 but showing a significant decline to 1908.41 Tg in 2022. Monthly and seasonal variations in the OBB carbon emissions from each region exhibited substantial differences. Of the 14 regions, the annual contribution of SHAF, the largest global contributor of OBB carbon emissions (32.74 %), increased by $2.70\,\%\,\mathrm{yr^{-1}}$, with the peak emissions of 283.59 Tg occurring in August 2021. SHAF has emerged as a primary contributor to global OBB carbon emissions owing to its substantial biomass and escalating human activities. Abundant biomass, including dense vegetation and rich forest resources, provides ample fuel for carbon emissions that are exacerbated by intensifying human activities (Chen et al., 2017). In August, specific meteorological conditions, such as high temperatures and low humidity facilitated the increased combustibility of biomass, resulting in a peak in carbon emissions (Shea et al., 1996). Although the SHAF region consistently remained the largest contributor to global OBB carbon emissions during 2020–2022, its annual emissions remained relatively stable, with minor fluctuations. Conversely, emissions from SHSA decreased at a rate of $105.22\,\mathrm{Tg\,yr^{-1}}$ from 2020 to 2022, with peak monthly emissions over the 3 years reaching 184.63,

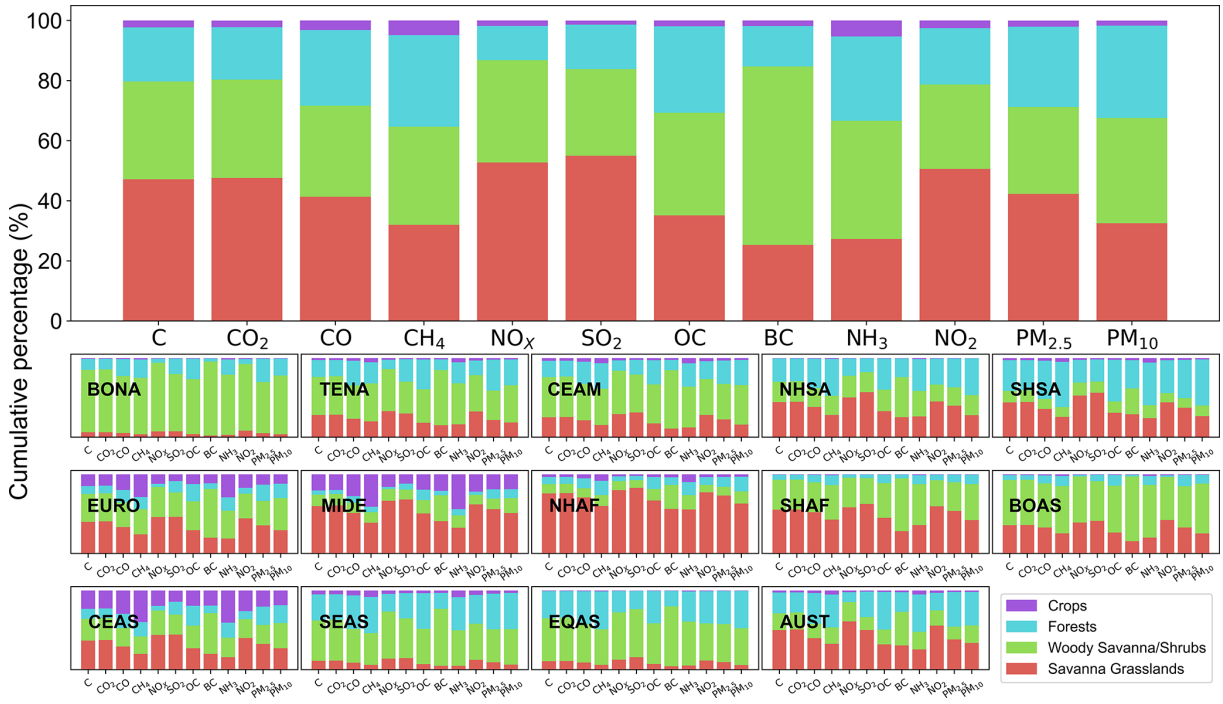

Figure 3. Cumulative percentage of annual OBB emissions for each land type in each region during 2020–2022.

222.12, and 123.98 Tg, respectively, where the size and status of emissions are consistent with Griffin et al. (2023). Annual C emissions in NHAF also declined, decreasing by 55.44 Tg over the 3 years, with its emissions accounting for the lowest percentage at 13.76 % in 2021.

Cumulatively, SHAF, SHSA, and NHAF represent almost 70 % of the global OBB carbon emissions, a testament to the profound intertwining of their native ecosystems, land utilization, and climatic influences on biomass combustion (Roy et al., 2022). Deeper exploration revealed that the SHAF, which is endowed with vast stretches of savannas and grasslands, undergoes intermittent dry periods (Hoffmann and Jackson, 2000). This climatic pattern, combined with entrenched agricultural customs like slash and burn, renders the region prone to wildfires (Lourenco et al., 2022). In the SHSA, which covers significant portions of the Amazon rainforest, rampant deforestation often involves controlled burning (Kröger and Nygren, 2020). Unfortunately, these sometimes escalate beyond the level of control, substantially adding to emission figures (Eufemia et al., 2022). In contrast, NHAF's shifting land-use paradigms coupled with increasingly recurrent droughts – potentially a byproduct of global warming – intensify the frequency of fires in the area (Machete and Dintwe, 2023).

Examination of monthly emissions data revealed significant regional disparities. For example, every January, NHAF, influenced by its monsoon cycles (Martin and Thorncroft, 2014), consistently emerges as the primary contributor to biomass carbon emissions, accounting for contributions of 50.74 %, 81.16 %, and 67.66 % across the 3 years, as reported by Tsivlidou et al. (2023). By March, SEAS witnessed a surge in emissions, largely due to shifts in forestry practices (Shi et al., 2014), with contributions escalating to 50.82 %, 57.78 %, and 40.67 % in subsequent years (Pletcher et al., 2022), respectively. The peak biomass carbon emissions in 2020 occurred in September, reaching 500.62 Tg. However, the peaks in 2021 and 2022 appeared sooner in August, with emissions of 729.37 and 357.57 Tg, respectively. The 2021 ascent of BONA emissions might be linked to altered land-use guidelines or increased farming activities (Zerriffi et al., 2023) and the many wildfires that occurred (Hoffman et al., 2022), while California's heightened investment in fire mitigation programs (Umunnakwe et al., 2022) and the US Forest Service's implementation of a decade-long strategy (Confronting the Wildfire Crisis, 2023) in 2022 have effectively curbed wildfire incidents in the TENA region. This shift in the perception of forest fire management has been instrumental in mitigating wildfire risk in the area. Nevertheless, it is important to acknowledge that the occurrence of wildfires varies over time (Bowman et al., 2017).

Figure 5 shows the notable temporal fluctuations in global wildfire carbon emissions for different fire types throughout the study period, from 2020 to 2022. Global combustion exhibited the highest carbon emissions in August and September. In September 2020, single-month emissions peaked at 500.62 Tg C. However, in 2021 and 2022, the zenith of carbon emissions from fires occurred in August, registering at 729.37 and 357.57 Tg, respectively. The smaller peaks ob-

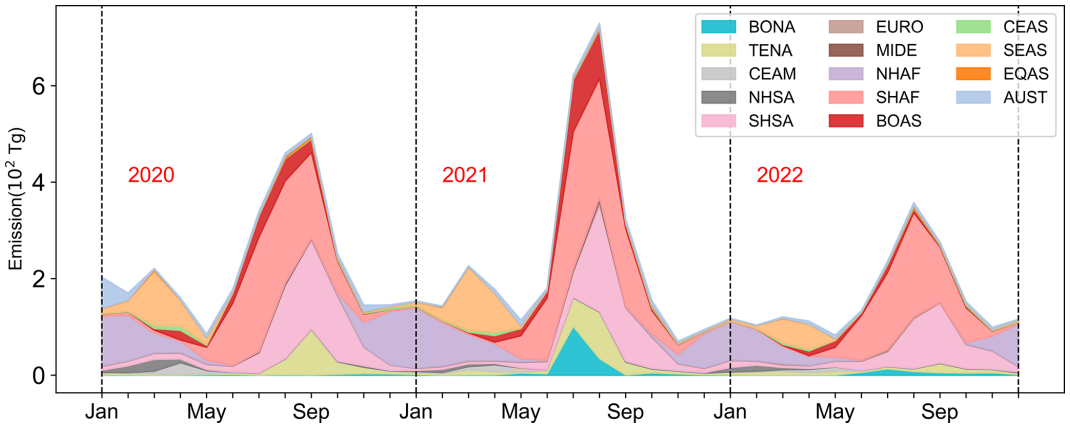

Figure 4. Global OBB carbon emissions in different regions during 2020–2022.

served in March should not be overlooked. Interestingly, although the timing of these emission peaks varied, their main contributing factors remained similar. In September, the daily carbon emission peaks from savanna grasslands, woody savanna/shrubs, and tropical forest regions were 7.54 (38 %), 7.12 (37 %), and 3.36 (31 %) Tg C d^{-1}, respectively. These sources constituted the primary contributors to the global biomass-combustion carbon emissions from July to October.

Spatial and temporal variations in global OBB emissions are pronounced because of the differences in ecosystems, climatic conditions, and human activities across different regions (Moritz et al., 2012; Ward et al., 2018). For instance, areas with expansive tropical grasslands, such as sub-Saharan Africa and Australia, typically experience high levels of OBB emissions because of the prevalence of both natural and anthropogenic fire activities (Williams et al., 2019; B. Zheng et al., 2021). Moreover, many regions undergo cyclical OBB emission patterns, which coincide with the onset of the dry and wet seasons (Dury et al., 2011; Gautam et al., 2013). The dry season, characterized by an increase in dry biomass and conducive weather conditions, often witnesses a surge in fire activity, resulting in elevated emission levels (Z. Zhang et al., 2023). These considerable spatial and temporal fluctuations in global OBB emissions mirror the diversity of ecosystems and climatic conditions across various geographic locations (Fagre et al., 2003), which are further influenced by human endeavours and natural fire regimes (Jones et al., 2022).

In 2020 and 2021, significant wildfire events, such as the California wildfires and Australian forest fires, led to an escalation in carbon emissions from fires (Collins et al., 2021, 2022; Gallagher et al., 2021; Keeley and Syphard, 2021; Safford et al., 2022). However, a dual phenomenon was observed in 2022. The implementation of robust wildfire control measures contributed to a reduction in emissions (Wollstein et al., 2022); however, an overall augmentation in annual precipitation led to a reduction in the degree of drought (Thackeray et al., 2022; X. Zhang et al., 2023). Consequently, the annual OBB carbon emissions in 2022 were lower than those in the preceding years.

Specifically, carbon emissions resulting from fire events were analysed in 14 global subregions from 2020 to 2022 (Fig. 6). This analysis revealed the primary sources of carbon emissions from fires worldwide and provided insights into the main constituents of combustion in different regions. Emission patterns across different global regions vary both temporally and spatially. The top three most emitting regions were SHAF, SHSA, and NHAF, which were closely associated with global emission trends, representing the main source of the emission peak in August and the emission during the winter months. During 2020 to 2022, the OBB conditions in the SHAF, SHSA, and NHAF regions have been relatively stable, with daily peak values of 12.04, 9.81, and 4.38 Tg, respectively. For SHAF and SHSA, burning activities were predominantly observed from July to September, which can be attributed to a combination of dry weather, strong winds, and specific meteorological conditions (Eames et al., 2023; Li et al., 2023). These factors collectively enhanced the combustibility of the biomass during this period, leading to an increased likelihood of burning. In SHAF, emissions were primarily influenced by savanna grasslands (49 %) and woody savanna/shrubs (47 %). Similarly, in SHSA, emissions were mainly affected by savanna grasslands (34 %) and tropical forests (38 %). While burning in the NHAF region is concentrated between November and January, primarily in January, this pattern is significantly influenced by the practice of slash-and-burn agriculture (Serrani et al., 2022), with savanna grasslands accounting for 77 % of the contributing factors.

CEAM and SEAS exhibited similar wildfire patterns, primarily occurring in March, and a noticeable decrease in burning activity emissions from 2020 to 2022. The predominant fire type in the CEAM region was woody savanna/shrubs (50 %), whereas in the SEAS region, it was mainly influenced by woody savanna/shrubs (50 %) and tropical forest (25 %). Overall, owing to similarities in factors, such as biomass fuel

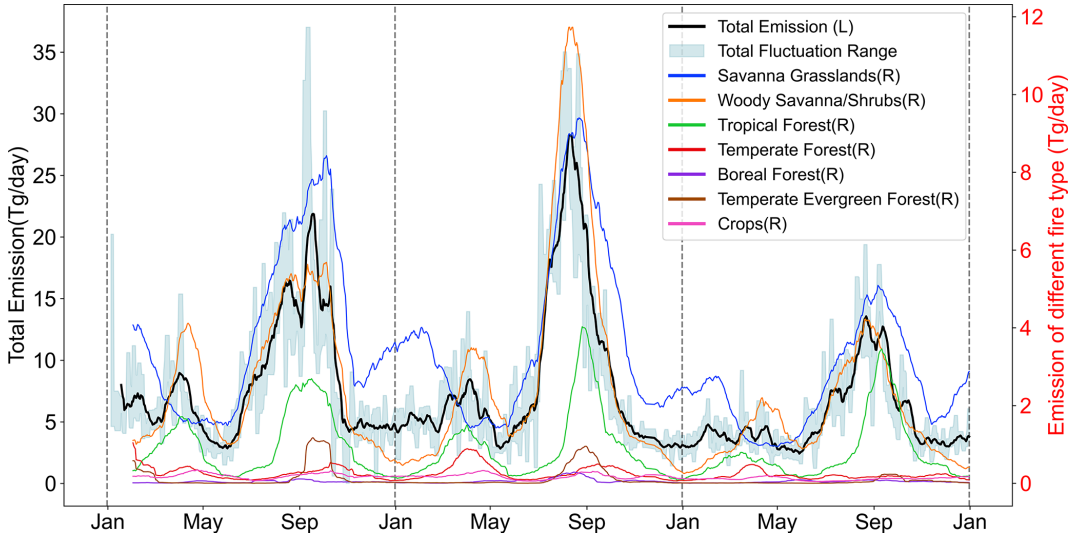

Figure 5. Variations in total global OBB carbon emissions and carbon emissions in different fire types across various regions from 2020 to 2022.

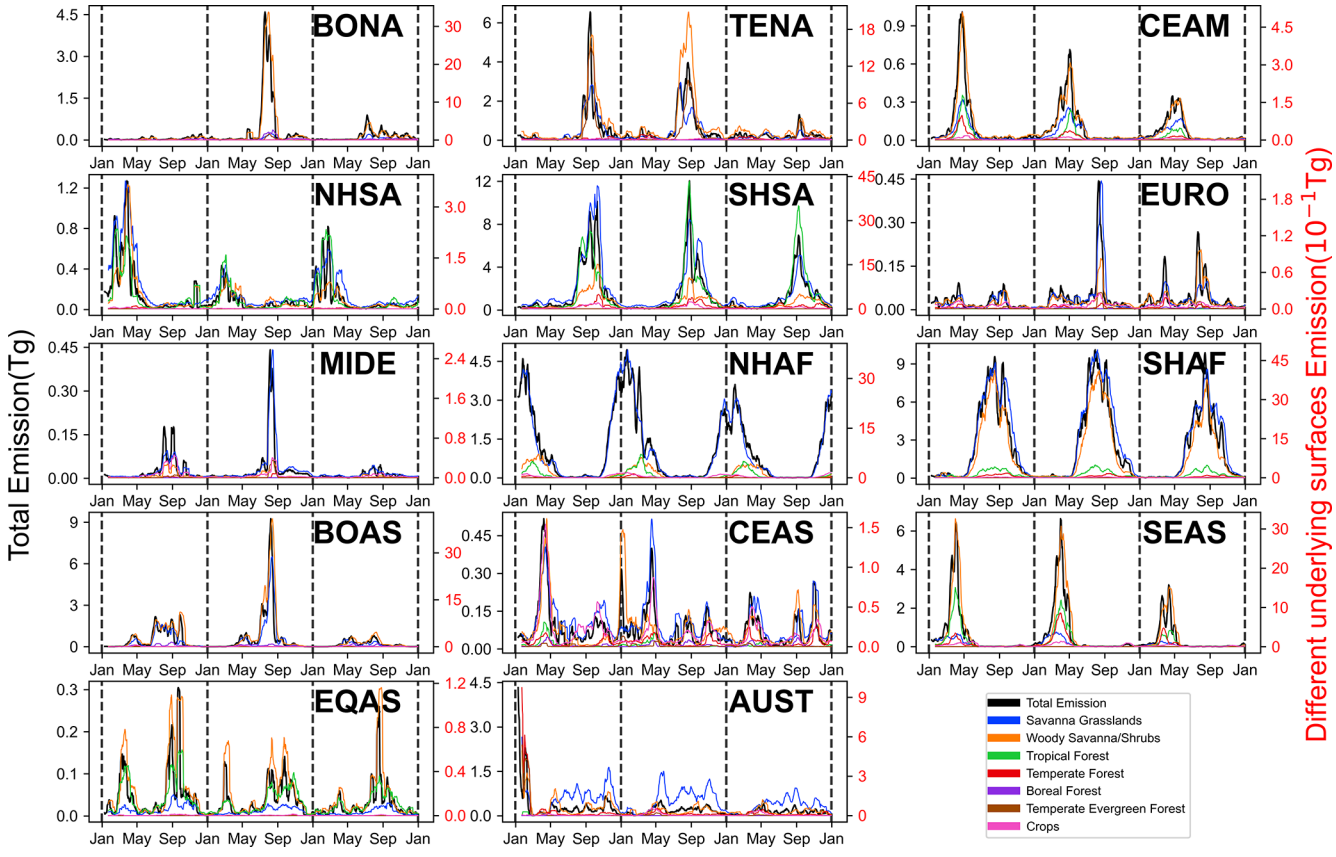

Figure 6. Global OBB emissions for different fire types in different regions (averaged over a 15 d window) from 2020 to 2022.

load and climate, the wildfire types in CEAM and SEAS were quite alike.

BONA, TENA, EURO, MIDE, BOAS, and AUST share a common characteristic: OBB carbon emissions exhibit a high degree of randomness, indicating their primary influence on natural wildfire events. For instance, British Columbia, Canada, experienced a series of wildfires in July 2021 (Copes-Gerbitz et al., 2022), leading to peak carbon emissions for BONA in 2021 (4.46 Tg). TENA, affected by a series of wildfires in the western United States in 2020 (Safford et al., 2022) and the ongoing wildfires in California in 2021 (Varga et al., 2022), showed elevated emissions in both years (6.12 Tg in 2020; 3.76 Tg in 2021), with woody savanna/shrubs being the main fire event type. For EURO, the apex of wildfires in 2021 was distinctly shaped by wildfires in southern and southeastern Europe (Tedim et al., 2022). The emissions were predominantly associated with the savanna grassland fire type (48 %). Moreover, in the BOAS region, wildfires were influenced by forest fires in Siberia (Ponomarev et al., 2022), where the principal fire type was woody savanna/shrubs (31 %). Regarding AUST, in January 2020, a significant forest fire event occurred (Storey et al., 2023), resulting in peak emissions of 4.48 Tg. The primary fire types were temperate forest (24 %) and savanna grassland (18 %).

The situation of OBB in CEAS is intricate. In March, substantial OBB emissions resulted from agricultural practices, such as slash-and-burn cultivation and the burning of crop residues (Liu and Shi, 2023), with crops being the predominant fire event type (30 %). In contrast, from August to November, OBB was mainly attributed to scorching weather and monsoon conditions (Shi et al., 2018), with savanna grasslands being the dominant type (28 %). Recently, owing to improvements in agricultural management practices, there has been a noticeable decrease in OBB events of crop types.

3.3 Cross-verification in different database

In this study, we juxtaposed the global distribution of OBB carbon emissions as estimated in GEIOBB with data published in the GFAS, GFED, and FEER datasets for 2020–2022 (Fig. 7). Overall, our assessments corresponded well with GFAS, GFED, and FEER; although there was an overestimation in high-latitude regions, the overall differences across large regions were minimal. For instance, we estimated the total carbon emissions in the BONA region to be 72.71 Tg, while the values from GFAS, GFED, and FEER were 61.21, 125.05, and 35.83 Tg, respectively. This variance can be attributed to the different resolutions (1 km × 1 km, 0.1° × 0.1°, 0.25° × 0.25°, and 0.1° × 0.1°) and different estimation methodologies employed. Both our study and GFED adopted an estimation approach based on the burned area, whereas GFAS and FEER formulated their inventories based on fire radiative energy. Consequently, our inventory yielded accurate assessment results and captured the spatial variation and heterogeneity of minor OBB emissions effectively, which could have been overlooked in coarse-scale analyses. Additionally, GFED utilizes MODIS satellite data to calculate the available biomass fuel, whereas we leverage the higher precision and small-fire quantification capability of FY-3D GFR data. Disparities between different satellite data and variations in parameter definitions during inventory formulation contribute to these differences. Moreover, we adopted published local-measurement-based emission factors and improved correlation coefficients for estimating OBB carbon emissions, which are more reliable and significantly enhance the local emission estimation accuracy.

Specifically, in high-emission regions (Fig. 8), such as NHAF, NHSA, and CEAS, our estimation of OBB carbon emissions (multi-year average of 394.25, 42.93, and 27.93 Tg; monthly peak average of 102.52, 11.86, and 6.24 Tg) aligned closely with those of GFED (multi-year average of 342.31, 29.10, and 38.16 Tg; monthly peak average of 97.58, 9.86, and 10.91 Tg) and GFAS (multi-year average of 288.81, 35.80, and 43.51 Tg; monthly peak average of 70.65, 9.64, and 9.82 Tg). However, discrepancies were observed between MIDE and EQAS, with FINN notably overestimating carbon emissions from fires. This overestimation by FINN is attributed to its methodology (Wiedinmyer et al., 2011), which relies on a combination of emission factors, conversion rates, and fire radiative energy values to estimate the emissions from agricultural residue burning. This contrasts with our approach, which bases estimates on the burned area and can thus accurately quantify carbon emissions from large fires and reduce uncertainty in fire data (Shi et al., 2020). Additionally, emission estimates during the periods by FINN, GFED, and GFAS were generated using data from the Terra and Aqua satellites, which captured data at 10:30 and 13:30 LT. However, the use of FY-3D, which captures data at 14:00 LT, proved highly effective in capturing such events. Furthermore, fire incidents tend to peak in the afternoon (Mehmood et al., 2022), with agricultural waste and crop residue burning more frequently occurring during this period due to higher temperatures that enhance burning efficiency (Jurdao et al., 2012). While, the average annual estimated OBB emissions exceed those reported by GFED by 617.14 $\mathrm{Tg\,C\,yr^{-1}}$. These discrepancies are probably related to small-scale fire events. For instance, the largest difference is observed in the SHAF region, exceeding those by GFED by 248.01 $\mathrm{Tg\,C\,yr^{-1}}$, followed by SHSA (190.28 $\mathrm{Tg\,C\,yr^{-1}}$) and SEAS (103.92 $\mathrm{Tg\,C\,yr^{-1}}$). In the SHAF region, compared to MODIS active fire, FY-3D GFR detects more small-fire points (Figs. S2 and S3a, b in the Supplement), which are isolated within 5 km resolution pixels. However, in this area, the majority of fire events are large-scale incidents, which means that although small fires are more numerous, they contribute minimally to the total emissions. Furthermore, fire events in SHSA (Fig. S3c and d) and SEAS (Fig. S3e and f) are primarily triggered by human activities consisting of small-scale incidents that are significantly linked to the overall emissions. In con-

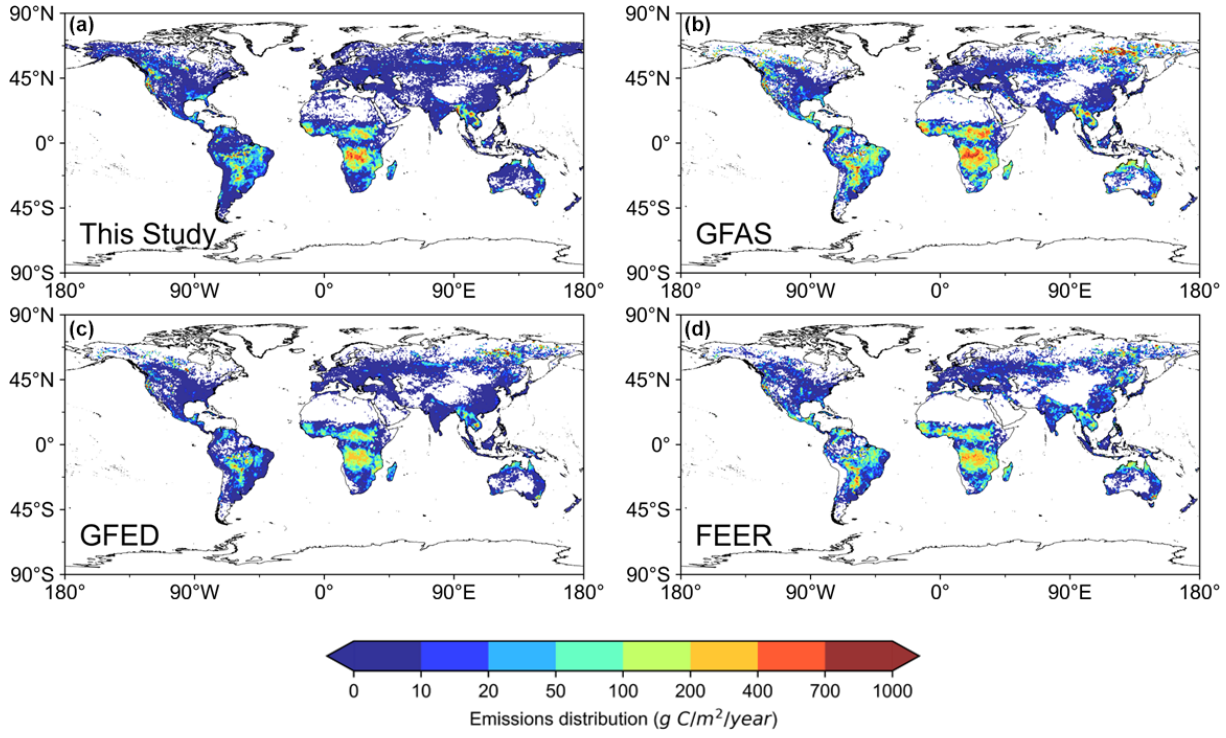

Figure 7. Comparison between this study **(a)** and other emission inventories **(b–d)** during 2020–2022 for average emissions at 0.5° resolution.

trast, areas frequently affected by large-scale fire events, such as TENA (99.05 Tg C yr^{-1}), NHAF (51.94 Tg C yr^{-1}), and other regions including NHSA, AUST, CEAM, MIDE, EURO, and EQAS, show relatively smaller discrepancies (all under 15.00 Tg C yr^{-1}).

The AGB values used in this study were directly derived from a dataset generated by combining field and satellite observations (Avitabile et al., 2016). GFED calculates this value through simulations using the biogeochemical Carnegie–Ames–Stanford Approach (CASA) model. While GFED has adjusted turnover rates for herbaceous leaves and surface litter at the ecosystem level to match the observed AGB used in this study, the significant differences in the estimated AGB between biogeochemical model simulations and field measurements are noteworthy (van der Werf et al., 2017). Furthermore, a high-resolution emissions inventory of 1 km × 1 km was developed. This inventory allows for the capture and description of spatial variations and heterogeneity of small-scale OBB emissions, providing detailed information on spatial discrepancies that may be missed by large-and-coarse-grid pixels (Shi et al., 2019).

We compared and validated the accuracy of monthly OBB carbon emission estimates in 14 global subregions using three global OBB fire products: GFAS, GFED, and FEER (Fig. 9). The Taylor diagram illustrates a high degree of consistency between these estimates and other inventories in terms of the standard deviation, correlation coefficient, and amplitude ratio. Overall, the results of this study were closer to the GFED and GFAS inventories, with the best agreement being observed with the GFAS inventory. Our results show a correlation coefficient of > 0.70 ($p < 0.01$) in over 80 % of the regions with the other three inventories, indicating a strong positive correlation and consistency in data trends between our study and the other three lists in most regions. Furthermore, in the top three emission source regions, SHAF, SHSA, and NHAF, our correlation coefficients with the other three emission inventories were all > 0.90, standard deviation ratios were < 2.00, and normalized centered root-mean-square errors were < 0.50. For example, compared with the other three inventories in the NHAF region, the correlation coefficients were all 0.97, with the standard deviations of 0.93 (GFED), 0.66 (GFAS), and 1.24 (FEER). However, when compared with the FEER inventory, there were still disparities in the estimated results between the FEER inventory and this study. For instance, in low-emission regions, such as EQAS, NHSA, CEAM, and MIDE, the correlation coefficients ranged from 0.60 to 0.95, with standard deviation exceeding 1.00. This was attributed to FEER's use of the FRP-based approach and overestimation in quantifying small-fire points (Ye et al., 2023).

In summary, we demonstrated that GEIOBB was a dataset with relatively high-quality estimates of global OBB emissions and that it performed well across all time periods and regions. Overall, a comparison with multiple inventories indicated that our GEIOBB model could effectively capture the

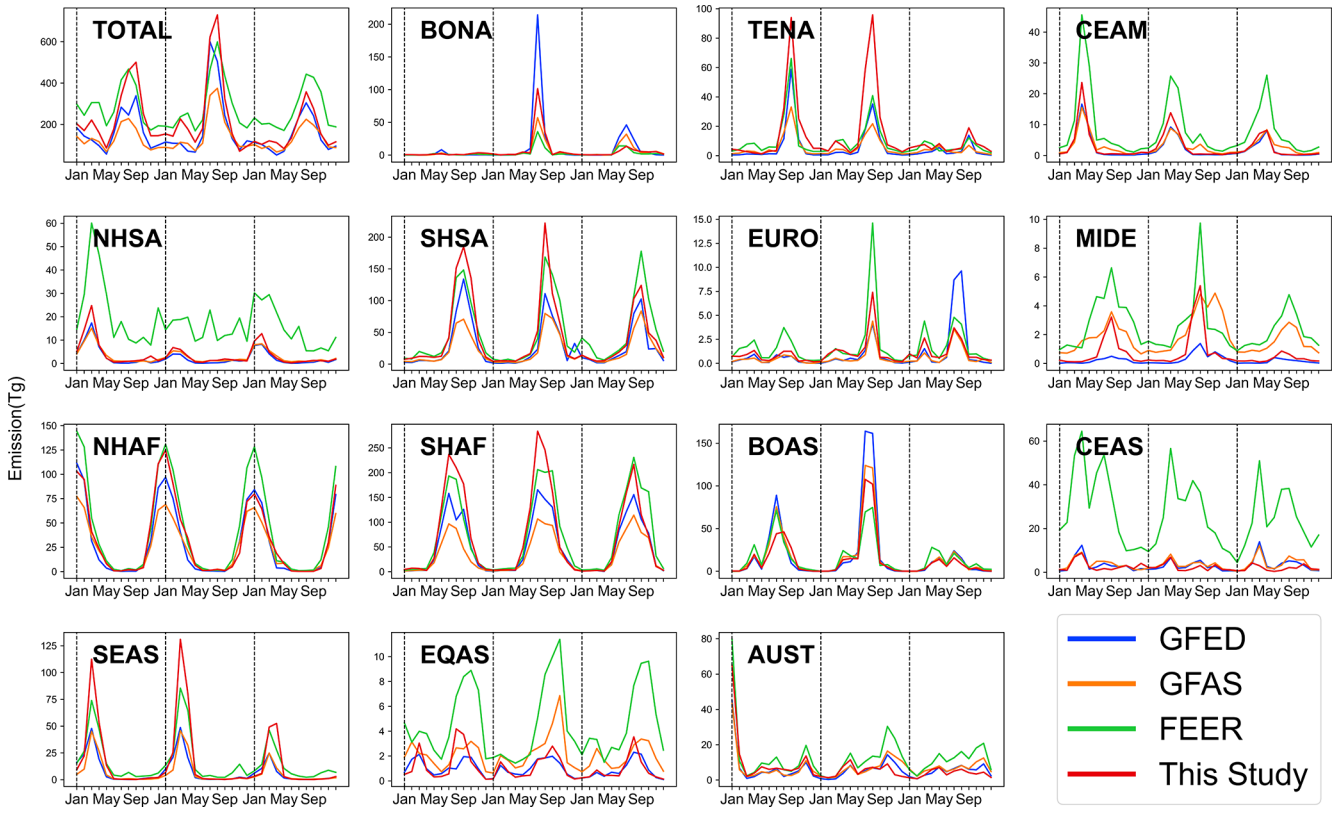

Figure 8. Comparison of monthly emissions in different regions of this and other emissions inventories.

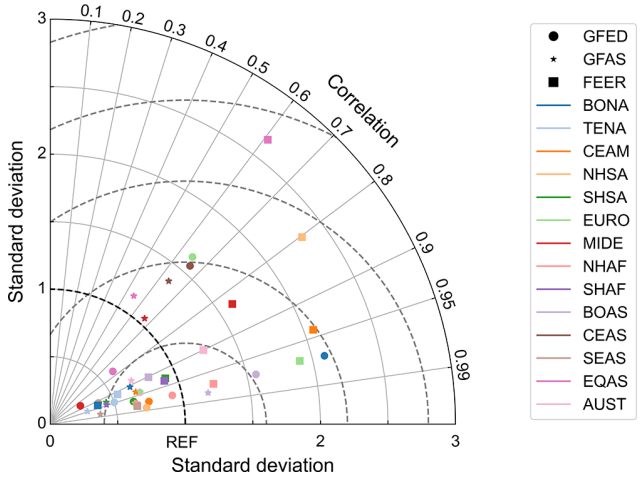

Figure 9. Normalized Taylor diagram plot of the comparison between GFED, GFAS, FEER, and this study regarding monthly OBB carbon emission values.

spatial and temporal distribution characteristics of OBB at large scales.

3.4 Advantages

To create a more accurate and effective biomass combustion carbon emission inventory, our research introduced three significant improvements compared to other inventory products. (1) The input global fire spot monitoring data from FY-3D showed a higher accuracy than MODIS in monitoring active fires (Xian et al., 2021). The OBB emissions exhibited significant consistency with the satellite fire detection results. Existing OBB emission estimation inventories differ mainly in the optimization of relevant parameters and estimation methods; however, they all rely on MODIS fire detection results as their primary data source. Our experiment utilized data from FY-3D GFR, which provides higher precision and the capability to quantify small-scale fire points more accurately (Yin et al., 2020). Consequently, the accuracy of the OBB carbon emissions assessment significantly improved. (2) Satellite and observational AGB resulted in less uncertainty than land-cover-based available biomass. Previous studies have used fixed values for AGB with regional and land-cover-based partitioning. Our research employed AGB inventory data, which, in contrast to the traditional method of regional sub-surface value assignment, better represent spatial varia-

tion trends. Additionally, by incorporating dynamic adjustment methods, we mitigated the temporal distribution shortcomings inherent in AGB data. This approach significantly enhances the portrayal of global biomass distribution across both time and space dimensions. (3) Spatially and temporally variable CF scaled by several vegetation indices can reflect a more accurate fraction of burned biomass than the allocated constants based on fire types. We optimized the previous single fixed value or simple formula-based definitions of CF by incorporating numerous parameters to better represent vegetation combustion conditions. To address the varying fire conditions, we performed a detailed subdivision based on different fire types. This advancement over conventional methods of fixed-value assignment or unified fixed-value methods without substrate distinction enables a more effective computation of burn factors for different types of fires, which can significantly enhance the delineation and understanding of burn factors in the biomass combustion process, paving the way for a more accurate carbon emission inventory. Through these notable improvements, our biomass combustion carbon emission inventory is a robust tool that provides precise and insightful analyses instrumental in advancing in the field of biomass combustion carbon emissions assessment.

3.5 Uncertainties

There were relatively high uncertainties in the estimation of OBB emissions for the seven types; the uncertainties were associated with the burned area, F, CF, and EF. Although the FY-3D GFR dataset is reliable for most OBB events, its resolution of 1 km results in poor detection performance for small-fire points (Zheng et al., 2023). The detected active fires were also underestimated due to cloud cover/thick smoke and omitted between satellite overpass, with an omission error of approximately 10 %–30 % (Giglio et al., 2006; Roberts et al., 2009; Schroeder et al., 2008). Furthermore, the diurnal cycle cannot be sufficiently represented using observations from polar orbiting satellites as these satellites have limited temporal coverage and may not capture the full range of fire activity throughout the day (Huang et al., 2024; Y. Zheng et al., 2021). Additionally, the uncertainties in the AGB calculations developed by Spawn and Gibbs (2020) ranged from 20 % to 80 %. More specifically, for approximately 80 % of the area, the AGB uncertainties were < 30 %, whereas in regions such as Africa and South America, high uncertainties of 60 %–70 % were observed. The estimated CF shows uncertainties of approximately 20 %–30 % based on empirical formulas (Zhang et al., 2008). The typical uncertainties for trace gas and aerosol emission factors for each land type, as compiled by Shi et al. (2015), ranged from 20 % to 50 %. Owing to the inherent uncertainties in all input parameters, after estimating the OBB emission inventories, we quantitatively assessed the estimation uncertainties in all emission species using 20 000 Monte Carlo simulations to calculate emission ranges with a 90 % confidence interval. Based on this, the emission ranges for different species are as follows: 1168.02–4120.83 Tg C, 2.31–5.48 Tg BC, 7.73–25.26 Tg CH_4, 193.11–505.66 Tg CO, 2994.71–14 153.75 Tg CO_2, 3.31–8.49 Tg of NH_3, 7.92–26.08 Tg NO_2, 12.70–26.87 Tg NO_x, 8.37–29.35 Tg OC, 37.66–84.17 Tg PM_{10}, 19.85–61.62 Tg $PM_{2.5}$, and 1.67–6.69 Tg SO_2.

4 Code and data availability

The GEIOBB dataset can be downloaded at http://figshare.com (last access: 30 July 2024) with the following DOI: https://doi.org/10.6084/m9.figshare.24793623.v2 (Liu et al., 2023).

5 Conclusion

We developed a high-spatial-resolution (1 km × 1 km grid) daily inventory of global OBB emissions. Our inventory used the updated satellite-based burned area product (FY-3D GFR), observational and satellite-based AGB, and vegetation-index-based spatiotemporally variable combustion efficiency data to estimate global OBB carbon emissions. The average annual estimated OBB emissions for 2020–2022 were 2586.88 Tg C, 8841.45 Tg CO_2, 382.96 Tg CO, 15.83 Tg CH_4, 18.42 Tg NO_x, 4.07 Tg SO_2, 18.68 Tg OC, 3.77 Tg BC, 5.24 Tg NH_3, 15.85 Tg NO_2, 42.46 Tg $PM_{2.5}$, and 56.03 Tg PM_{10}.

Taking carbon emission as an example, the average annual estimated OBB emissions were 72.71 Tg for BONA, 165.72 Tg for TENA, 34.11 Tg for CEAM, 42.93 Tg for NHSA, 520.54 Tg for SHSA, 13.02 Tg for EURO, 8.37 Tg for MIDE, 394.32 Tg for NHAF, 847.03 Tg for SHAF, 167.35 Tg for BOAS, 27.93 Tg for CEAS, 197.29 Tg for SEAS, 13.20 Tg for EQAS, and 82.37 Tg for AUST. NHAF, as the primary contributor in January, accounted for 50.74 %, 81.16 %, and 67.66 % in the 3 respective years. During the first peak of the years, March was mainly influenced by increased SEAS emissions (50.82 % in 2020, 57.78 % in 2021, and 40.67 % in 2022). In 2020, the annual peak occurred in September at 500.62 Tg, while in 2021 and 2022, it shifted to August, reaching 729.37 and 357.57 Tg, respectively. Peaks from savanna grasslands, woody savanna/shrubs, and tropical forest regions were 7.54 (38.37 %), 7.12 (37.42 %), and 3.36 Tg (31.01 %), respectively.

We demonstrated that savanna grassland contributed the largest portion (46.74 %) of total emissions, followed by woody savanna/shrubs (33.04 %) and tropical forest (12.11 %). Total OBB carbon emissions were the highest from SHAF, followed by SHSA and NHAF. The fire types where fires occurred were predominantly savanna grasslands, woody savanna/shrubs, and tropical forest in SHAF, SHSA, and NHAF and woody savanna/shrubs in SEAS. Further-

more, our data indicate a pronounced seasonal trend in carbon emissions. Regions such as the SHAF, SHSA, and TENA played pivotal roles, accounting for the surge in global carbon emissions observed in August.

Our high-spatial-resolution multi-species emissions inventory and spatiotemporal characteristics analysis will provide scientific and reliable evidence for formulating carbon emission policies and assessing temporal emission variation. Effective control of the savanna grasslands fire in SHAF, SHSA, and NHAF, as well as tropical forest fires in SHSA and woody savanna/shrubs fires in SHAF can greatly reduce carbon emissions. Moreover, this carbon emission inventory can be used for identifying regional biogeochemical circulation, atmospheric chemical simulations, and environmental health impacts. The accuracy and depth of our findings further underscore the potential for combining our bottom-up approach with top-down satellite observational methods, paving the way for refinement in future studies.

Supplement. The supplement related to this article is available online at: https://doi.org/10.5194/essd-16-3495-2024-supplement.

Author contributions. YL and YS produced GEIOBB. JC, WZ, GW, and TS conducted the data processing. YL, YS, and JC conceived the paper. YL and YS conducted data analysis and produced figures. YL and YS wrote the draft. YL, YS, TS, and JC reviewed and revised the paper.

Competing interests. The contact author has declared that none of the authors has any competing interests.

Disclaimer. Publisher's note: Copernicus Publications remains neutral with regard to jurisdictional claims made in the text, published maps, institutional affiliations, or any other geographical representation in this paper. While Copernicus Publications makes every effort to include appropriate place names, the final responsibility lies with the authors.

Acknowledgements. The authors extend their thanks to the anonymous reviewers for the valuable comments. This research is supported by the State Key Laboratory of Remote Sensing Science of Aerospace Information Research Institute and Innovation Center for FengYun Meteorological Satellite of National Satellite Meteorological Center.

Financial support. This research is supported by the National Key Research and Development Program of China (grant no. 2023YFB3907404), FY-3 Lot 03 Meteorological Satellite Engineering Ground Application System Ecological Monitoring and Assessment Application Project phase I (grant no. ZQC-R22227), and National Natural Science Foundation of China (grant no. 42071398).

Review statement. This paper was edited by Bo Zheng and reviewed by two anonymous referees.

References

Akagi, S. K., Yokelson, R. J., Wiedinmyer, C., Alvarado, M. J., Reid, J. S., Karl, T., Crounse, J. D., and Wennberg, P. O.: Emission factors for open and domestic biomass burning for use in atmospheric models, Atmos. Chem. Phys., 11, 4039–4072, https://doi.org/10.5194/acp-11-4039-2011, 2011.

Anderson, G. K., Sandberg, D. V., and Norheim, R. A.: Fire emission production simulator (FEPS) user's guide, USDA Forest Service, https://www.frames.gov/catalog/6921 (last access: 31 July 2024), 2004.

Avitabile, V., Herold, M., Heuvelink, G. B. M., Lewis, S. L., Phillips, O. L., Asner, G. P., Armston, J., Ashton, P. S., Banin, L., Bayol, N., Berry, N. J., Boeckx, P., de Jong, B. H. J., DeVries, B., Girardin, C. A. J., Kearsley, E., Lindsell, J. A., Lopez-Gonzalez, G., Lucas, R., Malhi, Y., Morel, A., Mitchard, E. T. A., Nagy, L., Qie, L., Quinones, M. J., Ryan, C. M., Ferry, S. J. W., Sunderland, T., Laurin, G. V., Gatti, R. C., Valentini, R., Verbeeck, H., Wijaya, A., and Willcock, S.: An integrated pan-tropical biomass map using multiple reference datasets, Global Change Biol., 22, 1406–1420, https://doi.org/10.1111/gcb.13139, 2016.

Baccini, A., Goetz, S. J., Walker, W. S., Laporte, N. T., Sun, M., Sulla-Menashe, D., Hackler, J., Beck, P. S. A., Dubayah, R., Friedl, M. A., Samanta, S., and Houghton, R. A.: Estimated carbon dioxide emissions from tropical deforestation improved by carbon-density maps, Nat. Clim. Change, 2, 182–185, https://doi.org/10.1038/nclimate1354, 2012.

Bowman, D. M. J. S., Williamson, G. J., Abatzoglou, J. T., Kolden, C. A., Cochrane, M. A., and Smith, A. M. S.: Human exposure and sensitivity to globally extreme wildfire events, Nat. Ecol. Evol., 1, 1–6, https://doi.org/10.1038/s41559-016-0058, 2017.

Bray, C. D., Battye, W., Aneja, V. P., Tong, D. Q., Lee, P., and Tang, Y.: Ammonia emissions from biomass burning in the continental United States, Atmos. Environ., 187, 50–61, https://doi.org/10.1016/j.atmosenv.2018.05.052, 2018.

Cao, G., Zhang, X., Wang, Y., and Zheng, F.: Estimation of emissions from field burning of crop straw in China, Chinese Sci. Bull., 53, 784–790, https://doi.org/10.1007/s11434-008-0145-4, 2008.

Chang, D. and Song, Y.: Estimates of biomass burning emissions in tropical Asia based on satellite-derived data, Atmos. Chem. Phys., 10, 2335–2351, https://doi.org/10.5194/acp-10-2335-2010, 2010.

Chen, J., Li, C., Ristovski, Z., Milic, A., Gu, Y., Islam, M. S., Wang, S., Hao, J., Zhang, H., He, C., Guo, H., Fu, H., Miljevic, B., Morawska, L., Thai, P., Lam, Y. F., Pereira, G., Ding, A., Huang, X., and Dumka, U. C.: A review of biomass burning: Emissions and impacts on air quality, health and climate in China, Sci. Total Environ., 579, 1000–1034, https://doi.org/10.1016/j.scitotenv.2016.10.146, 2017.

Chen, J., Yao, Q., Chen, Z., Li, M., Hao, Z., Liu, C., Zheng, W., Xu, M., Chen, X., Yang, J., Lv, Q., and Gao, B.: The Fengyun-3D (FY-3D) global active fire product: principle, methodology and validation, Earth Syst. Sci. Data, 14, 3489–3508, https://doi.org/10.5194/essd-14-3489-2022, 2022.

Chen, Y., Morton, D. C., Jin, Y., Collatz, G. J., Kasibhatla, P. S., van der Werf, G. R., DeFries, R. S., and Randerson, J. T.: Long-term trends and interannual variability of forest, savanna and agricultural fires in South America, Carbon Manag., 4, 617–638, https://doi.org/10.4155/cmt.13.61, 2013.

Chen, Y., Morton, D. C., Andela, N., van der Werf, G. R., Giglio, L., and Randerson, J. T.: A pan-tropical cascade of fire driven by El Niño/Southern Oscillation, Nat. Clim. Change, 7, 906–911, https://doi.org/10.1038/s41558-017-0014-8, 2017.

Cochrane, M. A. and Laurance, W. F.: Fire as a large-scale edge effect in Amazonian forests, J. Trop. Ecol., 18, 311–325, https://doi.org/10.1017/S0266467402002237, 2002.

Collins, L., Bradstock, R. A., Clarke, H., Clarke, M. F., Nolan, R. H., and Penman, T. D.: The 2019/2020 mega-fires exposed Australian ecosystems to an unprecedented extent of high-severity fire, Environ. Res. Lett., 16, 044029, https://doi.org/10.1088/1748-9326/abeb9e, 2021.

Collins, L., Clarke, H., Clarke, M. F., McColl Gausden, S. C., Nolan, R. H., Penman, T., and Bradstock, R.: Warmer and drier conditions have increased the potential for large and severe fire seasons across south-eastern Australia, Global Ecol. Biogeogr., 31, 1933–1948, https://doi.org/10.1111/geb.13514, 2022.

Confronting the Wildfire Crisis: https://www.fs.usda.gov/managing-land/wildfire-crisis, last access: 12 October 2023.

Copes-Gerbitz, K., Hagerman, S. M., and Daniels, L. D.: Transforming fire governance in British Columbia, Canada: an emerging vision for coexisting with fire, Reg. Environ. Change, 22, 48, https://doi.org/10.1007/s10113-022-01895-2, 2022.

De Sales, F., Xue, Y., and Okin, G. S.: Impact of burned areas on the northern African seasonal climate from the perspective of regional modeling, Clim. Dynam., 47, 3393–3413, https://doi.org/10.1007/s00382-015-2522-4, 2016.

DiMiceli, C., Sohlberg, R., and Townshend, J.: MODIS/Terra Vegetation Continuous Fields Yearly L3 Global 250 m SIN Grid V061, https://doi.org/10.5067/MODIS/MOD44B.061, 2022.

Dury, M., Hambuckers, A., Warnant, P., Henrot, A., Favre, E., Ouberdous, M., and François, L.: Responses of European forest ecosystems to 21(st) century climate: assessing changes in interannual variability and fire intensity, iForest, 82–99, https://doi.org/10.3832/ifor0572-004, 2011.

Eames, T., Russell-smith, J., Yates, C., Vernooij, R., and van der Werf, G.: Seasonal skew of tropical savanna fires, EGU General Assembly 2023, Vienna, Austria, 23–28 Apr 2023, EGU23-13544, https://doi.org/10.5194/egusphere-egu23-13544, 2023.

Eufemia, L., Dias Turetta, A. P., Bonatti, M., Da Ponte, E., and Sieber, S.: Fires in the Amazon Region: Quick Policy Review, Dev. Policy Rev., 40, e12620, https://doi.org/10.1111/dpr.12620, 2022.

Fagre, D. B., Peterson, D. L., and Hessl, A. E.: Taking the Pulse of Mountains: Ecosystem Responses to Climatic Variability, Climatic Change, 59, 263–282, https://doi.org/10.1023/A:1024427803359, 2003.

Fagua, J. C. and Ramsey, R. D.: Geospatial modeling of land cover change in the Chocó-Darien global ecoregion of South America; One of most biodiverse and rainy areas in the world, PLOS ONE, 14, e0211324, https://doi.org/10.1371/journal.pone.0211324, 2019.

Fang, Z., Deng, W., Zhang, Y., Ding, X., Tang, M., Liu, T., Hu, Q., Zhu, M., Wang, Z., Yang, W., Huang, Z., Song, W., Bi, X., Chen, J., Sun, Y., George, C., and Wang, X.: Open burning of rice, corn and wheat straws: primary emissions, photochemical aging, and secondary organic aerosol formation, Atmos. Chem. Phys., 17, 14821–14839, https://doi.org/10.5194/acp-17-14821-2017, 2017.

Filizzola, C., Falconieri, A., Lacava, T., Marchese, F., Masiello, G., Mazzeo, G., Pergola, N., Pietrapertosa, C., Serio, C., and Tramutoli, V.: Fire characterization by using an original RST-based approach for fire radiative power (FRP) computation, Fire, 6, 48, https://doi.org/10.3390/fire6020048, 2023.

Flannigan, M. D., Krawchuk, M. A., de Groot, W. J., Wotton, B. M., and Gowman, L. M.: Implications of changing climate for global wildland fire, Int. J. Wildland Fire, 18, 483–507, https://doi.org/10.1071/WF08187, 2009.

Friedl, M. and Sulla-Menashe, D.: MODIS/Terra+Aqua Land Cover Type Yearly L3 Global 500 m SIN Grid V061, https://doi.org/10.5067/MODIS/MCD12Q1.061, 2022.

Gallagher, R. V., Allen, S., Mackenzie, B. D. E., Yates, C. J., Gosper, C. R., Keith, D. A., Merow, C., White, M. D., Wenk, E., Maitner, B. S., He, K., Adams, V. M., and Auld, T. D.: High fire frequency and the impact of the 2019–2020 megafires on Australian plant diversity, Divers. Distrib., 27, 1166–1179, https://doi.org/10.1111/ddi.13265, 2021.

Gautam, R., Hsu, N. C., Eck, T. F., Holben, B. N., Janjai, S., Jantarach, T., Tsay, S.-C., and Lau, W. K.: Characterization of aerosols over the Indochina peninsula from satellite-surface observations during biomass burning pre-monsoon season, Atmos. Environ., 78, 51–59, https://doi.org/10.1016/j.atmosenv.2012.05.038, 2013.

Giglio, L., Csiszar, I., and Justice, C. O.: Global distribution and seasonality of active fires as observed with the Terra and Aqua Moderate Resolution Imaging Spectroradiometer (MODIS) sensors, J. Geophys. Res.-Biogeo., 111, G02016, https://doi.org/10.1029/2005JG000142, 2006.

Giglio, L., Schroeder, W., and Justice, C. O.: The collection 6 MODIS active fire detection algorithm and fire products, Remote Sens. Environ., 178, 31–41, https://doi.org/10.1016/j.rse.2016.02.054, 2016.

Griffin, D., Chen, J., Anderson, K., Makar, P., McLinden, C. A., Dammers, E., and Fogal, A.: Towards an improved understanding of wildfire CO emissions: a satellite remote-sensing perspective, EGUsphere [preprint], https://doi.org/10.5194/egusphere-2023-649, 2023.

Hoffman, K. M., Christianson, A. C., Gray, R. W., and Daniels, L.: Western Canada's new wildfire reality needs a new approach to fire management, Environ. Res. Lett., 17, 061001, https://doi.org/10.1088/1748-9326/ac7345, 2022.

Hoffmann, W. A. and Jackson, R. B.: Vegetation–Climate Feedbacks in the Conversion of Tropical Savanna to Grassland, J. Climate, 13, 1593–1602, https://doi.org/10.1175/1520-0442(2000)013<1593:VCFITC>2.0.CO;2, 2000.

Huang, J., Loría-Salazar, S. M., Deng, M., Lee, J., and Holmes, H. A.: Assessment of smoke plume height products derived from multisource satellite observations using lidar-derived height met-

rics for wildfires in the western US, Atmos. Chem. Phys., 24, 3673–3698, https://doi.org/10.5194/acp-24-3673-2024, 2024.

Ichoku, C. and Ellison, L.: Global top-down smoke-aerosol emissions estimation using satellite fire radiative power measurements, Atmos. Chem. Phys., 14, 6643–6667, https://doi.org/10.5194/acp-14-6643-2014, 2014.

Ichoku, C., Ellison, L. T., Willmot, K. E., Matsui, T., Dezfuli, A. K., Gatebe, C. K., Wang, J., Wilcox, E. M., Lee, J., Adegoke, J., Okonkwo, C., Bolten, J., Policelli, F. S., and Habib, S.: Biomass burning, land-cover change, and the hydrological cycle in Northern sub-Saharan Africa, Environ. Res. Lett., 11, 095005, https://doi.org/10.1088/1748-9326/11/9/095005, 2016.

Ito, A. and Penner, J. E.: Global estimates of biomass burning emissions based on satellite imagery for the year 2000, J. Geophys. Res.-Atmos., 109, D14S05, https://doi.org/10.1029/2003JD004423, 2004.

Jegasothy, E., Hanigan, I. C., Van Buskirk, J., Morgan, G. G., Jalaludin, B., Johnston, F. H., Guo, Y., and Broome, R. A.: Acute health effects of bushfire smoke on mortality in Sydney, Australia, Environ. Int., 171, 107684, https://doi.org/10.1016/j.envint.2022.107684, 2023.

Jones, M. W., Abatzoglou, J. T., Veraverbeke, S., Andela, N., Lasslop, G., Forkel, M., Smith, A. J. P., Burton, C., Betts, R. A., van der Werf, G. R., Sitch, S., Canadell, J. G., Santín, C., Kolden, C., Doerr, S. H., and Le Quéré, C.: Global and Regional Trends and Drivers of Fire Under Climate Change, Rev. Geophys., 60, e2020RG000726, https://doi.org/10.1029/2020RG000726, 2022.

Jurdao, S., Chuvieco, E., and Arevalillo, J. M.: Modelling Fire Ignition Probability from Satellite Estimates of Live Fuel Moisture Content, Fire Ecol., 8, 77–97, https://doi.org/10.4996/fireecology.0801077, 2012.

Kaiser, J. W., Heil, A., Andreae, M. O., Benedetti, A., Chubarova, N., Jones, L., Morcrette, J.-J., Razinger, M., Schultz, M. G., Suttie, M., and van der Werf, G. R.: Biomass burning emissions estimated with a global fire assimilation system based on observed fire radiative power, Biogeosciences, 9, 527–554, https://doi.org/10.5194/bg-9-527-2012, 2012.

Kanabkaew, T. and Kim Oanh, N. T.: Development of Spatial and Temporal Emission Inventory for Crop Residue Field Burning, Environ. Model. Assess., 16, 453–464, https://doi.org/10.1007/s10666-010-9244-0, 2011.

Keeley, J. E. and Syphard, A. D.: Large California wildfires: 2020 fires in historical context, Fire Ecol., 17, 22, https://doi.org/10.1186/s42408-021-00110-7, 2021.

Kolden, C. A., Abatzoglou, J. T., Jones, M. W., and Jain, P.: Wildfires in 2023, Nat. Rev. Earth Environ., 5, 238–240, https://doi.org/10.1038/s43017-024-00544-y, 2024.

Kröger, M. and Nygren, A.: Shifting frontier dynamics in Latin America, J. Agrar. Change, 20, 364–386, https://doi.org/10.1111/joac.12354, 2020.

Li, F., Zhu, Q., Riley, W. J., Zhao, L., Xu, L., Yuan, K., Chen, M., Wu, H., Gui, Z., Gong, J., and Randerson, J. T.: AttentionFire_v1.0: interpretable machine learning fire model for burned-area predictions over tropics, Geosci. Model Dev., 16, 869–884, https://doi.org/10.5194/gmd-16-869-2023, 2023.

Li, W., Li, M., Shi, C., Fang, R., Zhao, Q., Meng, X., Yang, G., and Bai, W.: GPS and BeiDou Differential Code Bias Estimation Using Fengyun-3C Satellite Onboard GNSS Observations, Remote Sens.-Basel, 9, 1239, https://doi.org/10.3390/rs9121239, 2017.

Li, X., Wang, S., Duan, L., Hao, J., Li, C., Chen, Y., and Yang, L.: Particulate and Trace Gas Emissions from Open Burning of Wheat Straw and Corn Stover in China, Environ. Sci. Technol., 41, 6052–6058, https://doi.org/10.1021/es0705137, 2007.

Liu, X., Zhang, Y., Huey, L. G., Yokelson, R. J., Wang, Y., Jimenez, J. L., Campuzano-Jost, P., Beyersdorf, A. J., Blake, D. R., Choi, Y., St. Clair, J. M., Crounse, J. D., Day, D. A., Diskin, G. S., Fried, A., Hall, S. R., Hanisco, T. F., King, L. E., Meinardi, S., Mikoviny, T., Palm, B. B., Peischl, J., Perring, A. E., Pollack, I. B., Ryerson, T. B., Sachse, G., Schwarz, J. P., Simpson, I. J., Tanner, D. J., Thornhill, K. L., Ullmann, K., Weber, R. J., Wennberg, P. O., Wisthaler, A., Wolfe, G. M., and Ziemba, L. D.: Agricultural fires in the southeastern U. S. during SEAC4RS: Emissions of trace gases and particles and evolution of ozone, reactive nitrogen, and organic aerosol, J. Geophys. Res.-Atmos., 121, 7383–7414, https://doi.org/10.1002/2016JD025040, 2016.

Liu, Y. and Shi, Y.: Estimates of Global Forest Fire Carbon Emissions Using FY-3 Active Fires Product, Atmosphere, 14, 1575, https://doi.org/10.3390/atmos14101575, 2023.

Liu, Y., Goodrick, S., and Heilman, W.: Wildland fire emissions, carbon, and climate: Wildfire–climate interactions, Forest Ecol. Manag., 317, 80–96, https://doi.org/10.1016/j.foreco.2013.02.020, 2014.

Liu, Y., Jie, C., Shi, Y., Zheng, W., Shan, T., and Wang, G.: Global Emissions Inventory from Open Biomass Burning (GEIOBB): Utilizing Fengyun-3D global fire spot monitoring data, Figshare [data set], https://doi.org/10.6084/m9.figshare.24793623.v2, 2023.

Lourenco, M., Woodborne, S., and Fitchett, J. M.: Fire regime of peatlands in the Angolan Highlands, Environ. Monit. Assess., 195, 78, https://doi.org/10.1007/s10661-022-10704-6, 2022.

Machete, R. L. and Dintwe, K.: Cyclic Trends of Wildfires over Sub-Saharan Africa, Fire, 6, 71, https://doi.org/10.3390/fire6020071, 2023.

Martin, E. R. and Thorncroft, C. D.: The impact of the AMO on the West African monsoon annual cycle, Q. J. Roy. Meteor. Soc., 140, 31–46, https://doi.org/10.1002/qj.2107, 2014.

Mehmood, K., Bao, Y., Saifullah, Bibi, S., Dahlawi, S., Yaseen, M., Abrar, M. M., Srivastava, P., Fahad, S., and Faraj, T. K.: Contributions of Open Biomass Burning and Crop Straw Burning to Air Quality: Current Research Paradigm and Future Outlooks, Front. Environ. Sci., 10, 852492, https://doi.org/10.3389/fenvs.2022.852492, 2022.

Moritz, M. A., Parisien, M.-A., Batllori, E., Krawchuk, M. A., Van Dorn, J., Ganz, D. J., and Hayhoe, K.: Climate change and disruptions to global fire activity, Ecosphere, 3, art49, https://doi.org/10.1890/ES11-00345.1, 2012.

Murdiyarso, D. and Lebel, L.: Local to global perspectives on forest and land fires in Southeast Asia, Mitig. Adapt. Strat. Gl., 12, 3–11, https://doi.org/10.1007/s11027-006-9055-4, 2007.

Nepstad, D. C., Verssimo, A., Alencar, A., Nobre, C., Lima, E., Lefebvre, P., Schlesinger, P., Potter, C., Moutinho, P., Mendoza, E., Cochrane, M., and Brooks, V.: Large-scale impoverishment of Amazonian forests by logging and fire, Nature, 398, 505–508, https://doi.org/10.1038/19066, 1999.

Nguyen, H. M., He, J., and Wooster, M. J.: Biomass burning CO, PM and fuel consumption per unit burned area estimates derived

across Africa using geostationary SEVIRI fire radiative power and Sentinel-5P CO data, Atmos. Chem. Phys., 23, 2089–2118, https://doi.org/10.5194/acp-23-2089-2023, 2023.

Pivello, V. R.: The Use of Fire in the Cerrado and Amazonian Rainforests of Brazil: Past and Present, Fire Ecol., 7, 24–39, https://doi.org/10.4996/fireecology.0701024, 2011.

Pletcher, E., Staver, C., and Schwartz, N. B.: The environmental drivers of tree cover and forest–savanna mosaics in Southeast Asia, Ecography, 2022, e06280, https://doi.org/10.1111/ecog.06280, 2022.

Ponomarev, E., Zabrodin, A., and Ponomareva, T.: Classification of Fire Damage to Boreal Forests of Siberia in 2021 Based on the dNBR Index, Fire, 5, 19, https://doi.org/10.3390/fire5010019, 2022.

Puliafito, S. E., Bolaño-Ortiz, T., Berná, L., and Pascual Flores, R.: High resolution inventory of atmospheric emissions from livestock production, agriculture, and biomass burning sectors of Argentina, Atmos. Environ., 223, 117248, https://doi.org/10.1016/j.atmosenv.2019.117248, 2020.

Qiu, X., Duan, L., Chai, F., Wang, S., Yu, Q., and Wang, S.: Deriving High-Resolution Emission Inventory of Open Biomass Burning in China based on Satellite Observations, Environ. Sci. Technol., 50, 11779–11786, https://doi.org/10.1021/acs.est.6b02705, 2016.

Richardson, D., Black, A. S., Irving, D., Matear, R. J., Monselesan, D. P., Risbey, J. S., Squire, D. T., and Tozer, C. R.: Global increase in wildfire potential from compound fire weather and drought, npj Clim. Atmos. Sci., 5, 1–12, https://doi.org/10.1038/s41612-022-00248-4, 2022.

Roberts, G., Wooster, M. J., and Lagoudakis, E.: Annual and diurnal african biomass burning temporal dynamics, Biogeosciences, 6, 849–866, https://doi.org/10.5194/bg-6-849-2009, 2009.

Roy, P. S., Ramachandran, R. M., Paul, O., Thakur, P. K., Ravan, S., Behera, M. D., Sarangi, C., and Kanawade, V. P.: Anthropogenic land use and land cover changes – a review on its environmental consequences and climate change, J Indian Soc. Remot., 50, 1615–1640, https://doi.org/10.1007/s12524-022-01569-w, 2022.

Saatchi, S. S., Harris, N. L., Brown, S., Lefsky, M., Mitchard, E. T. A., Salas, W., Zutta, B. R., Buermann, W., Lewis, S. L., Hagen, S., Petrova, S., White, L., Silman, M., and Morel, A.: Benchmark map of forest carbon stocks in tropical regions across three continents, P. Natl. Acad. Sci. USA, 108, 9899–9904, https://doi.org/10.1073/pnas.1019576108, 2011.

Safford, H. D., Paulson, A. K., Steel, Z. L., Young, D. J. N., and Wayman, R. B.: The 2020 California fire season: A year like no other, a return to the past or a harbinger of the future?, Global Ecol. Biogeogr., 31, 2005–2025, https://doi.org/10.1111/geb.13498, 2022.

Sahu, L. K. and Sheel, V.: Spatio-temporal variation of biomass burning sources over South and Southeast Asia, J. Atmos. Chem., 71, 1–19, https://doi.org/10.1007/s10874-013-9275-4, 2014.

Santana, V. M., Alday, J. G., Lee, H., Allen, K. A., and Marrs, R. H.: Modelling Carbon Emissions in Calluna vulgaris–Dominated Ecosystems when Prescribed Burning and Wildfires Interact, PLOS ONE, 11, e0167137, https://doi.org/10.1371/journal.pone.0167137, 2016.

Santiago-De La Rosa, N., González-Cardoso, G., Figueroa-Lara, J. de J., Gutiérrez-Arzaluz, M., Octaviano-Villasana, C., Ramírez-Hernández, I. F., and Mugica-Álvarez, V.: Emission factors of atmospheric and climatic pollutants from crop residues burning, J. Air Waste Manage., 68, 849–865, https://doi.org/10.1080/10962247.2018.1459326, 2018.

Scholes, M. and Andreae, M. O.: Biogenic and Pyrogenic Emissions from Africa and Their Impact on the Global Atmosphere, Ambio, 29, 23–29, 2000.

Schroeder, W., Csiszar, I., and Morisette, J.: Quantifying the impact of cloud obscuration on remote sensing of active fires in the Brazilian Amazon, Remote Sens. Environ., 112, 456–470, https://doi.org/10.1016/j.rse.2007.05.004, 2008.

Senande-Rivera, M., Insua-Costa, D., and Miguez-Macho, G.: Spatial and temporal expansion of global wildland fire activity in response to climate change, Nat. Commun., 13, 1208, https://doi.org/10.1038/s41467-022-28835-2, 2022.

Serrani, D., Cocco, S., Cardelli, V., D'Ottavio, P., Rafael, R. B. A., Feniasse, D., Vilanculos, A., Fernández-Marcos, M. L., Giosué, C., Tittarelli, F., and Corti, G.: Soil fertility in slash and burn agricultural systems in central Mozambique, J. Environ. Manage., 322, 116031, https://doi.org/10.1016/j.jenvman.2022.116031, 2022.

Shan, T. and Zheng, W.: Extraction method of burned area using GF-1 WFV images and FY-3D MERSI fire point products, Natl. Remote Sens. Bull., 28, 375–384, https://doi.org/10.11834/jrs.20221552, 2022.

Shea, R. W., Shea, B. W., Kauffman, J. B., Ward, D. E., Haskins, C. I., and Scholes, M. C.: Fuel biomass and combustion factors associated with fires in savanna ecosystems of South Africa and Zambia, J. Geophys. Res.-Atmos., 101, 23551–23568, https://doi.org/10.1029/95JD02047, 1996.

Shi, Y., Sasai, T., and Yamaguchi, Y.: Spatio-temporal evaluation of carbon emissions from biomass burning in Southeast Asia during the period 2001–2010, Ecol. Model., 272, 98–115, https://doi.org/10.1016/j.ecolmodel.2013.09.021, 2014.

Shi, Y., Matsunaga, T., and Yamaguchi, Y.: High-Resolution Mapping of Biomass Burning Emissions in Three Tropical Regions, Environ. Sci. Technol., 49, 10806–10814, https://doi.org/10.1021/acs.est.5b01598, 2015.

Shi, Y., Matsunaga, T., Yamaguchi, Y., Li, Z., Gu, X., and Chen, X.: Long-term trends and spatial patterns of satellite-retrieved $PM_{2.5}$ concentrations in South and Southeast Asia from 1999 to 2014, Sci. Total Environ., 615, 177–186, https://doi.org/10.1016/j.scitotenv.2017.09.241, 2018.

Shi, Y., Zhao, A., Matsunaga, T., Yamaguchi, Y., Zang, S., Li, Z., Yu, T., and Gu, X.: High-resolution inventory of mercury emissions from biomass burning in tropical continents during 2001–2017, Sci. Total Environ., 653, 638–648, https://doi.org/10.1016/j.scitotenv.2018.10.420, 2019.

Shi, Y., Zang, S., Matsunaga, T., and Yamaguchi, Y.: A multi-year and high-resolution inventory of biomass burning emissions in tropical continents from 2001–2017 based on satellite observations, J. Clean. Prod., 270, 122511, https://doi.org/10.1016/j.jclepro.2020.122511, 2020.

Spawn, S. A., and Gibbs, H. K.: Global Aboveground and Belowground Biomass Carbon Density Maps for the Year 2010, ORNL DAAC, Oak Ridge, Tennessee, USA [data set], https://doi.org/10.3334/ORNLDAAC/1763, 2020.

Stockwell, C. E., Veres, P. R., Williams, J., and Yokelson, R. J.: Characterization of biomass burning emissions from cooking fires, peat, crop residue, and other fuels with high-resolution

proton-transfer-reaction time-of-flight mass spectrometry, Atmos. Chem. Phys., 15, 845–865, https://doi.org/10.5194/acp-15-845-2015, 2015.

Storey, M. A., Price, O. F., and Fox-Hughes, P.: The influence of regional wind patterns on air quality during forest fires near Sydney, Australia, Sci. Total Environ., 905, 167335, https://doi.org/10.1016/j.scitotenv.2023.167335, 2023.

Tedim, F., Leone, V., Lovreglio, R., Xanthopoulos, G., Chas-Amil, M.-L., Ganteaume, A., Efe, R., Royé, D., Fuerst-Bjeliš, B., Nikolov, N., Musa, S., Milenković, M., Correia, F., Conedera, M., and Pezzatti, G. B.: Forest Fire Causes and Motivations in the Southern and South-Eastern Europe through Experts' Perception and Applications to Current Policies, Forests, 13, 562, https://doi.org/10.3390/f13040562, 2022.

Thackeray, C. W., Hall, A., Norris, J., and Chen, D.: Constraining the increased frequency of global precipitation extremes under warming, Nat. Clim. Chang., 12, 441–448, https://doi.org/10.1038/s41558-022-01329-1, 2022.

Tsivlidou, M., Sauvage, B., Bennouna, Y., Blot, R., Boulanger, D., Clark, H., Le Flochmoën, E., Nédélec, P., Thouret, V., Wolff, P., and Barret, B.: Tropical tropospheric ozone and carbon monoxide distributions: characteristics, origins, and control factors, as seen by IAGOS and IASI, Atmos. Chem. Phys., 23, 14039–14063, https://doi.org/10.5194/acp-23-14039-2023, 2023.

Umunnakwe, A., Parvania, M., Nguyen, H., Horel, J. D., and Davis, K. R.: Data-driven spatio-temporal analysis of wildfire risk to power systems operation, IET Generation, Transm. Distrib., 16, 2531–2546, https://doi.org/10.1049/gtd2.12463, 2022.

Urbanski, S.: Wildland fire emissions, carbon, and climate: Emission factors, Forest Ecol. Manag., 317, 51–60, https://doi.org/10.1016/j.foreco.2013.05.045, 2014.

van der Werf, G. R., Randerson, J. T., Giglio, L., Collatz, G. J., Kasibhatla, P. S., and Arellano Jr., A. F.: Interannual variability in global biomass burning emissions from 1997 to 2004, Atmos. Chem. Phys., 6, 3423–3441, https://doi.org/10.5194/acp-6-3423-2006, 2006.

van der Werf, G. R., Randerson, J. T., Giglio, L., Collatz, G. J., Mu, M., Kasibhatla, P. S., Morton, D. C., DeFries, R. S., Jin, Y., and van Leeuwen, T. T.: Global fire emissions and the contribution of deforestation, savanna, forest, agricultural, and peat fires (1997–2009), Atmos. Chem. Phys., 10, 11707–11735, https://doi.org/10.5194/acp-10-11707-2010, 2010.

van der Werf, G. R., Randerson, J. T., Giglio, L., van Leeuwen, T. T., Chen, Y., Rogers, B. M., Mu, M., van Marle, M. J. E., Morton, D. C., Collatz, G. J., Yokelson, R. J., and Kasibhatla, P. S.: Global fire emissions estimates during 1997–2016, Earth Syst. Sci. Data, 9, 697–720, https://doi.org/10.5194/essd-9-697-2017, 2017.

Varga, K., Jones, C., Trugman, A., Carvalho, L. M. V., McLoughlin, N., Seto, D., Thompson, C., and Daum, K.: Megafires in a Warming World: What Wildfire Risk Factors Led to California's Largest Recorded Wildfire, Fire, 5, 16, https://doi.org/10.3390/fire5010016, 2022.

Ward, D. S., Shevliakova, E., Malyshev, S., and Rabin, S.: Trends and Variability of Global Fire Emissions Due To Historical Anthropogenic Activities, Global Biogeochem. Cy., 32, 122–142, https://doi.org/10.1002/2017GB005787, 2018.

Wiedinmyer, C., Quayle, B., Geron, C., Belote, A., McKenzie, D., Zhang, X., O'Neill, S., and Wynne, K. K.: Estimating emissions from fires in North America for air quality modeling, Atmos. Environ., 40, 3419–3432, https://doi.org/10.1016/j.atmosenv.2006.02.010, 2006.

Wiedinmyer, C., Akagi, S. K., Yokelson, R. J., Emmons, L. K., Al-Saadi, J. A., Orlando, J. J., and Soja, A. J.: The Fire INventory from NCAR (FINN): a high resolution global model to estimate the emissions from open burning, Geosci. Model Dev., 4, 625–641, https://doi.org/10.5194/gmd-4-625-2011, 2011.

Wiedinmyer, C., Kimura, Y., McDonald-Buller, E. C., Emmons, L. K., Buchholz, R. R., Tang, W., Seto, K., Joseph, M. B., Barsanti, K. C., Carlton, A. G., and Yokelson, R.: The Fire Inventory from NCAR version 2.5: an updated global fire emissions model for climate and chemistry applications, Geosci. Model Dev., 16, 3873–3891, https://doi.org/10.5194/gmd-16-3873-2023, 2023.

Williams, A. P., Abatzoglou, J. T., Gershunov, A., Guzman-Morales, J., Bishop, D. A., Balch, J. K., and Lettenmaier, D. P.: Observed Impacts of Anthropogenic Climate Change on Wildfire in California, Earths Future, 7, 892–910, https://doi.org/10.1029/2019EF001210, 2019.

Wollstein, K., Creutzburg, M. K., Dunn, C., Johnson, D. D., O'Connor, C., and Boyd, C. S.: Toward integrated fire management to promote ecosystem resilience, Rangelands, 44, 227–234, https://doi.org/10.1016/j.rala.2022.01.001, 2022.

Wu, J., Kong, S., Wu, F., Cheng, Y., Zheng, S., Yan, Q., Zheng, H., Yang, G., Zheng, M., Liu, D., Zhao, D., and Qi, S.: Estimating the open biomass burning emissions in central and eastern China from 2003 to 2015 based on satellite observation, Atmos. Chem. Phys., 18, 11623–11646, https://doi.org/10.5194/acp-18-11623-2018, 2018.

Wu, M., Luo, J., Huang, T., Lian, L., Chen, T., Song, S., Wang, Z., Ma, S., Xie, C., Zhao, Y., Mao, X., Gao, H., and Ma, J.: Effects of African BaP emission from wildfire biomass burning on regional and global environment and human health, Environ. Int., 162, 107162, https://doi.org/10.1016/j.envint.2022.107162, 2022.

Xian, D., Zhang, P., Gao, L., Sun, R., Zhang, H., and Jia, X.: Fengyun meteorological satellite products for earth system science applications, Adv. Atmos. Sci., 38, 1267–1284, https://doi.org/10.1007/s00376-021-0425-3, 2021.

Yao, X., Tiantian, Q. U., Wenjing, C., Jun, Y. I. N., Yongjin, L. I., Zhenzhong, S. U. N., and Hui, Z.: Estimation of grassland biomass using MODIS data and plant community characteristics, Chin. J. Eco-Agric., 25, 530–541, https://doi.org/10.13930/j.cnki.cjea.160931, 2017.

Ye, X., Cheng, T., Li, X., and Zhu, H.: Impact of satellite AOD data on top-down estimation of biomass burning particulate matter emission, Sci. Total Environ., 864, 161055, https://doi.org/10.1016/j.scitotenv.2022.161055, 2023.

Yin, Z., Chen, F., Lin, Z., Yang, A., and Li, B.: Active fire monitoring based on FY-3D MERSI satellite data, Remote Sens. Technol. Appl., 35, 1099–1108, http://www.rsta.ac.cn/EN/10.11873/j.issn.1004-0323.2020.5.1099 (last access: 31 July 2024), 2020.

You, C. and Xu, C.: Delayed wildfires in 2020 promote snowpack melting in the western United States, P. Natl. Acad. Sci. USA, 120, e2218087120, https://doi.org/10.1073/pnas.2218087120, 2023.

Zerriffi, H., Reyes, R., and Maloney, A.: Pathways to sustainable land use and food systems in Canada, Sustain. Sci., 18, 389–406, https://doi.org/10.1007/s11625-022-01213-z, 2023.

Zhang, X., Kondragunta, S., Schmidt, C., and Kogan, F.: Near real time monitoring of biomass burning particulate emis-

sions ($PM_{2.5}$) across contiguous United States using multiple satellite instruments, Atmos. Environ., 42, 6959–6972, https://doi.org/10.1016/j.atmosenv.2008.04.060, 2008.

Zhang, X., Duan, J., Cherubini, F., and Ma, Z.: A global daily evapotranspiration deficit index dataset for quantifying drought severity from 1979 to 2022, Sci. Data, 10, 824, https://doi.org/10.1038/s41597-023-02756-1, 2023.

Zhang, Z., Zhang, L., Xu, H., Creed, I. F., Blanco, J. A., Wei, X., Sun, G., Asbjornsen, H., and Bishop, K.: Forest water-use efficiency: Effects of climate change and management on the coupling of carbon and water processes, Forest Ecol. Manag., 534, 120853, https://doi.org/10.1016/j.foreco.2023.120853, 2023.

Zheng, B., Ciais, P., Chevallier, F., Chuvieco, E., Chen, Y., and Yang, H.: Increasing forest fire emissions despite the decline in global burned area, Science Advances, 7, eabh2646, https://doi.org/10.1126/sciadv.abh2646, 2021.

Zheng, W. and Chen, J.: Fire monitoring based on FY-3D/MERSI-II far-infrared data, J. Infrared Millim. W., 39, 120–127, https://doi.org/10.11972/j.issn.1001-9014.2020.01.016, 2020.

Zheng, W., Chen, J., Yan, H., Liu, C., and Tang, S. H.: Global fire monitoring products of FY-3D/MERSI-II and their applications, J. Remote Sens., 24, 521–530, https://doi.org/10.11834/jrs.20209177, 2020.

Zheng, W., Chen, J., Liu, C., Shan, T., and Yan, H.: Study of the Application of FY-3D/MERSI-II Far-Infrared Data in Wildfire Monitoring, Remote Sens.-Basel, 15, 4228, https://doi.org/10.3390/rs15174228, 2023.

Zheng, Y., Liu, J., Jian, H., Fan, X., and Yan, F.: Fire Diurnal Cycle Derived from a Combination of the Himawari-8 and VIIRS Satellites to Improve Fire Emission Assessments in Southeast Australia, Remote Sens.-Basel, 13, 2852, https://doi.org/10.3390/rs13152852, 2021.

Zhou, Y., Xing, X., Lang, J., Chen, D., Cheng, S., Wei, L., Wei, X., and Liu, C.: A comprehensive biomass burning emission inventory with high spatial and temporal resolution in China, Atmos. Chem. Phys., 17, 2839–2864, https://doi.org/10.5194/acp-17-2839-2017, 2017.